Tensile failure model of carbon fibre in unidirectionally reinforced epoxy composites with mean-field homogenisation

Ling Wu[a,], Etienne Maillard[b], Ludovic Noels[a]

[a] *University of Liege, Department of Aeronautics and Mechanical Engineering, Computational & Multi-Scale Mechanics of Materials, Allée de la découverte 9, B-4000 Liège, Belgium*
[b] *SONACA S.A., Route Nationale 5, 6041 Gosselies, Belgium*

Abstract

This paper presents an extension of the so-called incremental-secant mean-field homogenisation (MFH) formulation accounting for fibre bundle failure and matrix cracking in Unidirectional (UD) composites. First a model for fibre bundle failure is developed based on the strength failure probability of the carbon fibre described by a Weibull distribution. This fibre bundle failure model is then framed in a damage model of embedded bundles in a matrix by considering an exponential relation to describe the longitudinal stress build-up profile experimentally observed during failure of embedded fibre bundles. Cracking of the matrix in UD composites is accounted for through an anisotropic non-local damage model, which allows capturing the so-called 0° splits experimentally observed during the longitudinal tension of UD plies. A Mean Field Homogenisation (MFH) model is then extended to account for these damage models as component behaviours of the 2-phase composite material. A finite element multi-scale simulation of a notched laminate shows that the intra-laminar failure modes observed by an *in situ* experiment reported in the literature are well captured by the damage variables related to the matrix and fibre bundle failure processes. Inter-laminar failure is also captured by an extrinsic cohesive law introduced between the plies.

Keywords: Mean-field homogenisation, Incremental-secant formulation, Fibre bundle failure, Matrix cracking, Unidirectional Composites

1. Introduction

In the context of unidirectional fibre reinforced composites, fibres, as the main load carrying component, dominate the failure of composite materials

Email addresses: l.wu@ulg.ac.be (Ling Wu), Etienne.Maillard@sonaca.com (Etienne Maillard), l.noels@ulg.ac.be (Ludovic Noels)

when plies are loaded along the longitudinal direction. Since the failure of fibre-reinforced composites often occurs suddenly, sometimes without any *prior* visible signs of damage, understanding and modelling the gradual development of microscopic damage in fibres and fibre bundles is vital to the safe application of composites.

In order to predict the failure of unidirectional composites, many experimental studies and numerical analyses have been carried out on the damage mechanism of fibre bundles embedded in a matrix. It is widely accepted and confirmed by experimental studies that the fibre strength is a stochastic property that also exhibits a size effect [1]. Using an established statistical description of the strength of fibre bundles, direct finite element simulations were applied on fibre reinforced matrix cells loaded along the fibre direction in order to evaluate the stress transfer and stress redistribution near the fibre bundle breaking point, as well as the formation of clusters of broken fibre bundles [2, 3, 4]. Optical microscopy has been used for *in situ* measurements of the progressive fibre bundle breakage and of the stress redistribution in the adjacent unbroken fibre bundles [5, 6]. High resolution computed tomography (CT) has also been used during carbon/epoxy composite laminates *in situ* tensile tests up to failure in order to study the 3D fibre failure process [7]. Because of these experiments and models, the mechanisms of fibre failure is now well understood for longitudinally loading composite material: i) the fibre bundle failure initiates as local fibre breakages and is accompanied by a redistribution of stress in the neighbouring fibre bundles; ii) the failure probability of neighbouring fibre bundles increases because of the stress concentrations; iii) the increased loading in the neighbouring fibre bundles causes the development of clusters of broken fibre bundles; and iv) the clusters number grows with the increase of the loading, until one of them becomes unstable, leading to the final failure of the composite material.

Some numerical models were developed in order to represent the fibre-failure of composite plies. Using a progressive failure model for fibre bundles, finite element analyses were applied on representative volume elements (RVEs) in [8]. A spring-element model was used to simulate the failure of fibres in 2D and 3D RVEs [9, 10, 11]. An efficient numerical scheme, based on a probabilistic analysis of the bundle failure, was proposed in [12]. Phase field approaches, which represent the crack surface topology through a diffusive crack zone governed by an auxiliary variable, were combined with smeared interfaces [13] in order to capture crack interface interactions. This combination allowed micro-mechanical models of fibre-matrix debonding and matrix cracking interaction to be developed [14]. In order to develop macro-scale constitutive models of composites failure, a damage model was developed in the framework of the thermodynamics of irreversible processes in [15] and phase field methods with two auxiliary variables, respectively for fibre and inter-fibre failures, were developed in [16] to simulate the crack propagation in UD-CFRP composites. However, with this latter approaches, the propagation of crack/damage zones in anisotropic media cannot always be captured correctly. In order to account for the anisotropic nature of UD plies in the phase field methods, and thus to predict the correct crack direction, a characteristic lengths tensor with preferred directions was in-

troduced in the phase-field equation governing the auxiliary variable together with a new definition of the driving energy release rate [17, 18], see also the recent review of phase field methods applied to composite laminates [19].

However, when considering macro-scale models, the parameters are identified by considering the response at the ply level and not directly from the constituents. Besides, the progressive failure mechanism of fibre bundles also interacts with the fibre-matrix interface debonding and with the matrix yielding and cracking during the failure process of composite materials [20, 6]. Modelling this gradual development of coupled microscopic degradation mechanisms and predicting such damage induced failure during macro-scale simulations remain challenging. Indeed, predicting the failure of composites with direct finite element analyses on RVE remains computationally too costly when all the coupled damage phenomena are considered while macro-scale models are not detailed enough to represent the interplay between these damage mechanisms, motivating the development of multi-scale approaches.

As an efficient semi-analytical micromechanics model, mean-field-homogenisation (MFH) makes it possible to apply damage-enhanced multi-scale analyses on real composite coupons [21]. By opposition to computational homogenisation, in MFH the microstructure is not explicitly represented but defined from the phases material properties, the phases volume fractions, and either from the inclusion geometrical shape or from their spatial correlation [22]. The homogenisation framework is then formulated by a series of equations, completed by the knowledge of phases properties, that can be solved iteratively.

A damage-enhanced elasto-plastic model has been considered in MFH to simulate the effect of the micro-cracks in the matrix phase [38, 39]. This matrix damage enriched MFH has been applied on UD fibre reinforced laminate coupons and the matrix induced damage modes were found to be in good agreement with micro-CT measurements [21]. In particular, the damage evolution in the matrix phase was formulated in an implicit non-local approach originally derived for isotropic materials [40, 41] in order to remove mesh-dependency during strain localisation. This implicit non-local method postulates that the damage diffusion is determined by a non-local variable, which is an auxiliary field of the finite element discretisation. This auxiliary field is solved through an additional Helmholtz equation dependent on a characteristic length. In the case of brittle materials, the implicit non-local model shares strong similarities, both in the mathematical and in the implementation points of view, with the phase-field method as discussed in [42, 43]. The advantage of the phase-field model for brittle materials is that the energy release rate explicitly appears in the auxiliary equations, while the parameters of the damage law have to be calibrated to recover the same results with the non-local approach [44]. However, the non-local approach allows considering easily arbitrary damage models for complex material behaviours. The non-local MFH formulation was extended in [21] to the case of anisotropic UD-fibre reinforced epoxy by introducing an anisotropic characteristic lengths tensor so that the fibres "block" the matrix material-point interactions in the transverse directions of UD-fibre and, on the contrary, "prolong" the interaction in the longitudinal direction. Because of this

anisotropic model, the damage propagates along the fibre directions even for longitudinally loaded plies, as observed in the micro-CT measurements, which is not necessarily the case with meso-scale continuum damage models [45]. Such an anisotropic characteristic length tensor was also introduced in the macro-scale phase-field formulation for UD laminates in [17, 18]. Nevertheless the damage-enhanced MFH was accounting neither for fibre failure nor for fibre-matrix interface debonding.

Because MFH is an efficient computational method that benefits from the advantages inherent to multi-scale methods, the three more important ones being the ability to be defined from the micro-constituent geometrical and material parameters only without recourse to macro-scale characterisation, its ability to account for the phases interactions in a physical way, and its ability to provide information on the phases material responses during the loading process, it is a good candidate to simulate the failure of composite laminates. However, the current existing framework can only capture matrix cracking [21]. The purpose of this work is to enrich the MFH to account for the fibre failure as well as the matrix cracking. To this end, we develop, on the one hand, a failure micro-mechanics model of embedded fibre bundle and, on the other hand, an extension of the MFH multi-scale model accounting for this fibre bundle failure. In particular, a stochastic fibre bundle damage model is first proposed based on a Weibull distribution of fibre strength [1]. This fibre bundle damage model is then embedded in the MFH method in order to simulate the response of UD composites up to the failure point. In the linear elastic range, an equivalent bonded inclusion (EqBI), which can be seen as a damaged inclusion, was proposed to replace the inclusions with a debonded interfaces in short fibre reinforced composites [46, 47]. The properties of the EqBI were estimated from the reduced capability of the stress transfer from the matrix to the inclusion due to the debonded interface. Using the same idea, a damage variable is here introduced to describe the progressive fibre bundle breaking and the degradation of stress carrying capability of the fibre bundles in the MFH model. However, this model considers the decrease of load carrying capability of the fibre in the longitudinal direction only, requiring the introduction of size-effect or characteristic fibre failure length in the model to capture the stress build-up profile. The debonding of fibre-matrix interfaces near the fibre breaking point and the debonding caused by transverse loading on the composites are captured by the damage in the matrix naturally. This approach is in agreement with the physics observed in composites with strong fibre/matrix interface. Indeed, scanning electron microscope (SEM) images taken from experimental tests performed in [48] on composites, with weak and strong fibre/matrix interfaces, show that the dominating failure mechanism in the case of a weak interface is a true interfacial failure while in the case of a strong interface the dominating failure mechanism is an inter-phase failure. After ultimate fracture of composite with strong interface, fibre surfaces are observed to be almost totally covered by the matrix in the inter-phase. Therefore, in the case of composites with strong interfaces, because the true failure mechanism is the matrix cracking, the failure of the matrix and of interfaces can be taken into account using a damage-enhanced constitutive

model for the matrix and the fibre-matrix interface debonding does not need to be explicitly modelled [49]. The ability of the developed MFH-based multi-scale model accounting for fibre failure and matrix cracking to capture the details of the damage mechanisms is then illustrated by simulating the failure of notched laminates for which the local failure modes are compared to experimental CT observations. In particular, both matrix and fibre dominant failure modes are captured by the model through the damage variables associated to the matrix and fibre failure mechanisms, respectively.

The paper is organised as follows. The damage model for fibre bundle failure is developed in Section 2. The effect of the characteristic failure length of the embedded fibre bundle is studied in Section 3, allowing its determination from experimental measurements. Section 4 details the extension of Mean-Field Homogenisation to account for both matrix cracking and fibre bundle failure. The developed multi-scale model is then applied in Section 5, first on a simple ply tension in order to evaluate the predicted ply strength, and then on a notched laminate, for which the damage and delamination distributions are compared to experimental observations obtained by micro-CT images and reported in the literature.

2. Damage model for carbon fibre bundle

A damage model is adopted to describe the progressive failure of fibres in a fibre bundle. The damage variable $D = 0$ indicates an intact fibre bundle, *i.e.* without broken fibres, and $D = 1$ represents a fully broken fibre bundle. In order to derive the damage evolution according to the loading process, the statistics of a single fibre strength is first studied before considering the failure process of a fibre bundle. Finally, the effect of the number of fibres in the bundle is studied.

2.1. Strength of single carbon fibre

The strength of carbon fibres is not unique and extensive experimental studies show that carbon fibres under tensile loading exhibit a statistical strength distribution, which can be described using a Weibull function of the following form

$$\Phi(\hat{\sigma},\, L) = 1.0 - \exp\left[-\left(\frac{L}{L_0}\right)^{\alpha}\left(\frac{\hat{\sigma}}{\sigma_0}\right)^{m}\right], \tag{1}$$

where $\Phi(\hat{\sigma},\, L)$ is the cumulative probability of failure of a fibre of gauge length L at a given stress level of $\hat{\sigma}$. The scale parameter σ_0 and the shape parameters α and m are experimentally-determined constants, and L_0 is the reference gauge length at which these parameters are determined.

2.2. Damage model of the bundle

2.2.1. The damage variable definition of a fibre bundle

Considering a fibre bundle of N fibres and of length L under longitudinal loading, at a given stress level $\hat{\sigma}$, the probability of having k fibres broken can

be described by a Binomial distribution

$$f(k,\, N,\, \varphi) = \begin{pmatrix} N \\ k \end{pmatrix} \varphi^k (1-\varphi)^{N-k}\,, \tag{2}$$

where $\begin{pmatrix} N \\ k \end{pmatrix}$ is the binomial coefficient $\frac{N!}{k!(N-k)!}$, and where φ is the probability of a single fibre to be broken. This probability is expressed at a given stress level $\hat{\sigma}$ by

$$\varphi = \mathcal{P}(\sigma_{\mathrm{u}} < \hat{\sigma},\, L) = \Phi(\hat{\sigma},\, L)\,, \tag{3}$$

where σ_{u} is the strength of a single fibre, where $\mathcal{P}$ is the probability measure, and where $\Phi(\hat{\sigma},\, L)$ is given by Eq. (1). When the number of fibres in a bundle is large enough, which is usually the case in UD composite materials, the Binomial distribution (2) can be approximated by a normal distribution $\mathcal{N}(N\varphi,\, N\varphi(1-\varphi))$ when φ is near neither to 0 nor to 1. The condition of this approximation can be stated by the 3-standard-deviation rule which requires

$$N > 9\frac{\varphi}{1-\varphi} \quad \text{and} \quad N > 9\frac{1-\varphi}{\varphi}\,. \tag{4}$$

Using the concept of damage mechanics, the damage variable D is defined by the ratio of broken fibres number to the total fibres number of the bundle and thus reads

$$D = \frac{k}{N}\,. \tag{5}$$

It can be seen that the evolution of D is not deterministic, and follows a probability distribution instead. The damage probability is deduced from Eq. (2) and its distribution can be approximated by the normal distribution [1]

$$\pi(D|\hat{\sigma},\, L) \approx \mathcal{N}\left(\varphi,\, \frac{\varphi(1-\varphi)}{N}\right)\,, \tag{7}$$

where $\varphi = \Phi(\hat{\sigma}\,, L)$ takes the expression of Eq. (1), and where $\mathcal{N}\left(\varphi,\, \frac{\varphi(1-\varphi)}{N}\right)$ stands for a normal distribution of average value φ and variance $\frac{\varphi(1-\varphi)}{N}$.

[1] For a given fibres number N, a critical stress for damage evolution can be set in order to make φ satisfying the lower boundary of Eq. (4). Using Eq. (1) and letting $\Phi(\sigma_{\mathrm{cr}},\, L) = \frac{9}{9+N}$ yield

$$\sigma_{\mathrm{cr}} = \sigma_0 \left[\left(\frac{L}{L_0}\right)^{-\alpha} \ln\left(\frac{9+N}{N}\right)\right]^{1/m}\,. \tag{6}$$

The 3-standard-deviation rule (4) is then always satisfied by considering $\hat{\sigma} > \sigma_{\mathrm{cr}}$ as a criterion for damage evolution.

Table 1: Weibull distribution parameters of AS4 carbon fibre [1].

L_0 (mm)	σ_0 (MPa)	α	m
10.0	4493	0.6	5.0

2.2.2. The damage variable evolution of a fibre bundle

In the probabilistic definition of the damage variable, we have assumed implicitly that the longitudinal stress $\hat{\sigma}$ is reached instantaneously and that the stress level $\hat{\sigma}$ represents the stress in the unbroken fibres. However during a progressive loading process, *e.g.* in a controlled displacement loading process, the breaking of fibres results in an unloading of the stress level in the fibre bundle considered as a whole. This means that the stress level $\hat{\sigma}$ in Eq. (7) is not the apparent stress σ of the fibre bundle during the damaging process, but the effective one, *i.e.* the one in the unbroken fibres. Therefore, considering an apparent longitudinal loading stress σ on a fibre bundle, the effective stress $\hat{\sigma}$ of the unbroken fibres is defined as,

$$\hat{\sigma} = \frac{\sigma}{(1-D)}\,, \tag{8}$$

which has to be used as argument in Eq. (7).

2.2.3. Handling of the damage variable uncertainty of a fibre bundle

From Eq. (7), it can be seen that the evolution of the damage variable D is a stochastic process according to the effective stress $\hat{\sigma}$ (8). The realisations of this damage evolution $D(\sigma)$ can be obtained when considering an incremental loading process. During each increment interval $[t_n,\, t_{n+1}]$, D^*_{n+1} is drawn from a normal distribution $\mathcal{N}\left(\varphi,\, \frac{\varphi(1-\varphi)}{N}\right)$ with $\varphi = \Phi\left(\hat{\sigma}_{n+1}\,, L\right)$ and $D_{n+1} = \max\left\{D_n,\, D^*_{n+1}\right\}$.

However, this stochastic damage evolution cannot be used in a finite element implicit resolution process because, on the one hand, the uncertainty should be spatially related and, on the other hand, the derivative of the damage variable to the strain does not have a deterministic expression. This problem can be solved by using the expectation $\mathbb{E}[D(\sigma)]$ instead of $D(\sigma)$. Spatial distribution of strength can be accounted for by using a constant realisation ϱ of the normal distribution $\mathcal{N}(0,1)$ at each Gauss point, leading to the following damage evolution at that Gauss point

$$D_\varrho = \varphi + \varrho\sqrt{\frac{\varphi(1-\varphi)}{N}} \quad \text{with} \quad \varphi = \Phi\left(\frac{\sigma}{1-D_\varrho},\, L\right)\,. \tag{9}$$

2.3. Effect of the number of fibres in the bundles

AS4 carbon fibre, a continuous high strength high strain fibre processed based on Polymerisation of AcryloNitrile (PAN), is used for the parametric study. The Weibull probability distribution parameters of AS4 carbon fibre

were identified in [1] and are listed in Table 1. The Length parameter L in Eq. (1) is set to be $100r$, where $r \approx 3.5\,\mu$m is the radius of an AS4 carbon fibre. The determination of the value of L, responsible for the size effect in the composite material, will be discussed in details in Section 3.

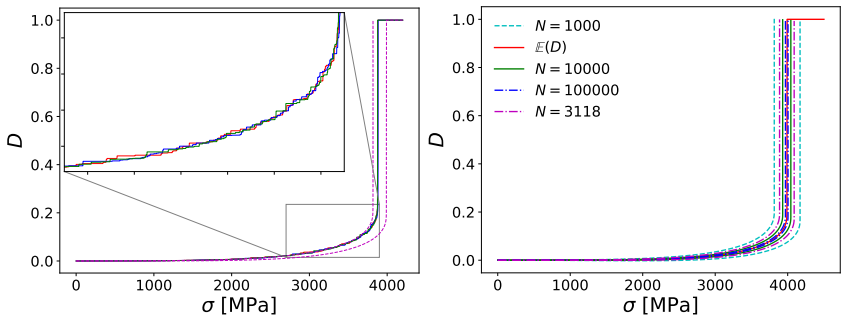

(a) (b)

Figure 1: Effect of the number of fibres in the bundles: (a) Three realisations of the stochastic damage evolution (7) for $N = 1000$ fibres; the "purple dashed lines" correspond to $D_{3.0}$ and $\mathbb{E}(D) = D_{0.0}$ of the damage evolution (9); and (b) The damage evolution (9) in fibre bundles of different fibres numbers N for $D_{3.0}$, $D_{-3.0}$ and $\mathbb{E}(D) = D_{0.0}$; Snapback after softening onset is not illustrated.

Since at a given loading σ, the damage D is not a deterministic value but follows a distribution approximated by the Normal distribution (7), three realisations of the damage evolution *vs.* the apparent stress curve are reported in Fig. 1(a) for $N = 1000$. The expectation and one of the upper 3-standard-deviation bound of the damage evolution (9), which is practically considered in the future finite element implementations, are also illustrated for comparison purpose. Because of the condition $D_{n+1} \geq D_n$, the stochastic damage evolution (7) tends to follow the path of fast evolution, as it can be seen in Fig. 1(a). Using Eq. (9), the 3-standard-deviation bounds and expectation of damage *vs.* apparent stress curves are plotted in Fig. 1(b) for $L = 0.35$ mm and the successive fibres numbers $N = 1000$, 10000, 100000 in the bundle. We also consider $N \approx 3118$, which corresponds to the number of fibres in a bundle corresponding to a composite material of cross-section $1 \times 0.2\,\text{mm}^2$ with volume fraction $v_{\text{I}} = 0.6$. Fig. 1(b) shows that with the increase of the number of fibres in a bundle, the damage evolution converges to the expectation $D(\sigma)$, which reads $\mathbb{E}[D(\sigma)] = D_{0.0}(\sigma)$.

3. Identification of the characteristic fibre failure length

Before applying the extended MFH model to a composite structural analysis, the fibre gauge length L used to defined the fibre failure probability in Eq. (1) needs to be identified. In Section 2.3, an assumed value of $L = 100r$

was considered for illustration purpose. In this section the value of L is identified from micro-structure measurements reported in the literature and from the considered material properties.

3.1. Fragments of a fibre embedded in the matrix

When a fibre embedded in a matrix is loaded under longitudinal tension, it first breaks at its weakest point. If the load on the composite material keeps increasing, the fibre breaks at its second weakest point, then at the third one, and so on, until matrix cracking occurs and ultimately the sample fails. This failure process has been experimentally observed [5]: microscopic measurements showed that a longitudinal drop in the fibre strain develops progressively at several locations during a tensile loading. From the physical point of view, the size of the fibre fragments at the final failure stage corresponds to the gauge length L needed to define the Weibull distribution (1).

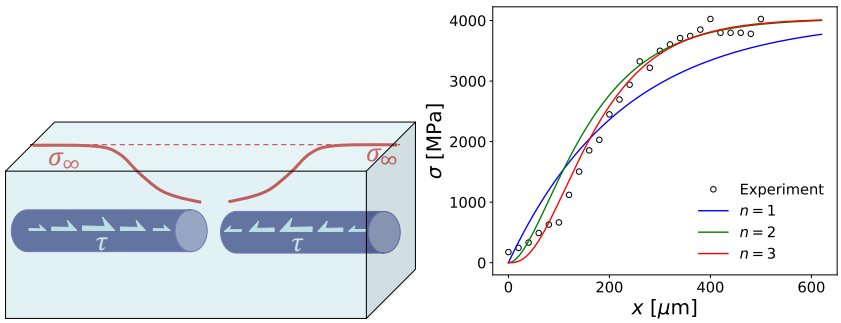

(a) Schematics (b) Stress profile

Figure 2: The longitudinal stress build-up at the adjacent parts of the fibre breaking point: (a) Schematics of the interface interaction; and (b) The longitudinal stress build-up a in broken fibre predicted by Eq. (10) for $cl = 227$, 113, 101 μm and, respectively, for $n = 1$, 2, 3, and comparison with the experimental measurements of Ref. [5].

3.2. Description of the stress profile of a broken embedded fibre

Once broken, the longitudinal stress in the fibre is no longer uniform but follows a stress build-up profile as illustrated in Fig. 2(a): while the longitudinal stress of the fibre vanishes at the breaking point, the stress can be recovered aft and forward of this point because of the action of the shear stress between the fibre and the matrix. The upcoming breaking points will take place at the parts where the longitudinal stress is at a high level. Therefore, the size of fibre fragments relies on the stress build-up profile of an embedded fibre. Extensive research has been carried out on the study of stress build-up profile of a broken embedded fibre either analytically, experimentally or numerically [50, 5, 51]. The analytical model, or shear-lag theory, is widely used to evaluate the stress build-up of a broken fibre embedded in an elastic matrix. This model can lead to a really high shear stress at fibre-matrix interface, which is not realistic in

the case of an elasto-plastic matrix. The analysis of experimental measurements [5, 51] has shown that the shear stress at fibre-matrix interface is limited by the yielding stress of the matrix. In [51], a piece-wise function was used to fit the experimental measurements of the stress build-up. The comparison between experimental measurements and finite element simulations accounting for the effect of fibre-matrix debonding and fibre-matrix interface friction has been carried out in [51]. Because of the multi-mechanism involved in fibre breaking of composites, such as fibre breaking, fibre-matrix debonding, fibre-matrix interface friction and stress wave propagation, it is not straightforward to reproduce the stress profile of a broken embedded fibre accurately even with direct finite element simulations.

Based on the experimental measurements provided in Ref. [5], a continuous function is proposed in this work to describe the stress profile of a broken embedded fibre, which reads

$$\sigma(x) = \sigma_\infty \left(1 - \exp\left(-\frac{|x|}{cl}\right)\right)^n , \tag{10}$$

where the origin of x is at the breaking point, σ_∞ is the maximum longitudinal tensile stress in the parts of the fibre far away from the breaking point, the parameter n controls the shape of stress build-up profile, and cl defines the effective range of the fibre breaking point. Since the shear stress can be set as $\tau = \frac{r}{2}\frac{\mathrm{d}\sigma}{\mathrm{d}x}$, where r is the radius of the fibre, the maximum shear stress at the fibre-matrix interface can be computed through Eq. (10) and expressed as

$$\tau_{\max} = \frac{nr\sigma_\infty}{2cl} \times \max_{x\in R}\left[\left(1 - \exp\left(-\frac{|x|}{cl}\right)\right)^{n-1} \exp\left(-\frac{|x|}{cl}\right)\right] . \tag{11}$$

This equation shows that the maximum shear stress at the fibre-matrix interface depends on both n and on the length parameter cl.

3.3. Determination of stress build-up parameters and length L for the Weibull fibre strength distribution.

The stress build-up parameters can be determined according to microscopic measurements and presented material properties of Ref. [5], such as the values of r and $\tau_{\max}$, with $r \approx 3.6\,\mu$m and $\tau_{\max} \approx 32$ MPa which is the yielding stress of the matrix phase. For assumed values of $n = 1, 2, 3$, Eq. (11) respectively simplifies into

$$\tau_{\max} = \frac{r\sigma_\infty}{2cl}, \quad \frac{r\sigma_\infty}{4cl}, \quad \frac{2r\sigma_\infty}{9cl} \quad \text{and} \tag{12}$$

$$cl = \frac{r\sigma_\infty}{2\tau_{\max}}, \quad \frac{r\sigma_\infty}{4\tau_{\max}}, \quad \frac{2r\sigma_\infty}{9\tau_{\max}} . \tag{13}$$

Fig. 2(b) compares the stress build-up profile predicted by Eq. (10) with the reproduced experimental measurements of Ref. [5], in which longitudinal Young's modulus of carbon fibre was $E_{\mathrm{I}}^3 = 350$ GPa and far-field stress was

$\sigma_\infty \approx 4035$ MPa. A good agreement with the experimental measurement of the stress build-up profile obtained using $n = 3$ in Eq. (10) is seen in Fig. 2(b), although the results with $n = 2$ are also acceptable too.

Finally we define the parameter L as the minimum positive value of x in Eq. (10) for which the broken fibre has recovered 99% of its longitudinal stress, yielding $L = 600\,\mu$m for $n = 2$, and $L = 580\,\mu$m for $n = 3$.

3.4. Discussion

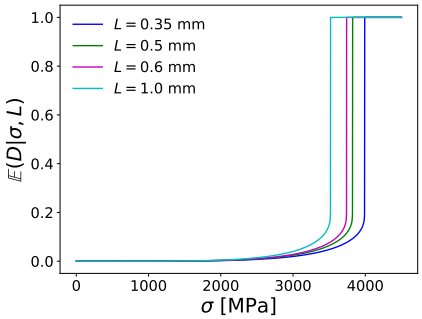

Figure 3: Expectations of the longitudinal damage evolution in AS4 fibre bundles for different values of the length parameter L; Snapback after softening onset is not illustrated.

Using the stochastic fibre bundle damage evolution (7), the expectations of damage evolution for AS4 carbon fibre bundles are computed respectively with $L = 0.35$, 0.5, 0.6, 1.0 mm using the properties of Table 1 and are reported in Fig. 3. This figure shows that a higher value of L leads to a lower strength of the fibre bundles.

According to the expression (10) of the stress build-up, in a broken fibre the longitudinal stress recovery rate is proportional to the parameter cl, or in short $L \propto cl$. Therefore, from Eq. (13), one has

$$L \propto \frac{r\sigma_\infty}{\tau_{\max}}\,, \tag{14}$$

which shows that the value of L depends on σ_∞. To remain simple, a constant σ_∞ can be used to yield a constant L. One possibility for σ_∞ is to consider $\sigma_\infty = \sigma_0$, see Eq. (1). Another possible choice for σ_∞ is to consider the expectation of the fibre tensile strength, *i.e.* $\sigma_\infty = \mathbb{E}[\sigma|L]$. According to the Weibull distribution (1), this yields a non-linear equation in L, which can be solved numerically. From the effects of r and $\tau_{\max}$ on L, it can be stated that a composite material made of fibres of small radius r and matrix of higher tensile yielding stress –which corresponds to a higher $\tau_{\max}$– has a higher longitudinal tensile strength since a lower value of L results in a higher value of the tensile strength as illustrated in Fig. 3.

4. MFH enhanced with matrix and fibres damage models

In this section we first recall the main idea of the Mean-Field Homogenisation (MFH) framework for linear and non-linear two-phase composite materials. The incremental-secant MFH method previously developed to account for damage evolution in the matrix phase is then extended to account for a local damage evolution in the inclusion phase. The fibre bundle damage model developed in Section 2 is then used to derive the damage evolution of the inclusion phase, while the damage evolution of the matrix relies on the previously developed non-local damage-enhanced elasto-plastic model [39, 21].

4.1. Mori-Tanaka-based MFH for composites

In this section, the basic theory and equations of the Mori-Tanaka extension of the Eshelby single inclusion solution [23] to multiple-inclusion interactions are recalled, first in the linear range and then in the non-linear range by defining a Linear Comparison Composite (LCC) material.

The MFH defines the relation between the macro-strains $\boldsymbol{\varepsilon}_{\mathrm{M}}$ and macro-stresses $\boldsymbol{\sigma}_{\mathrm{M}}$ through the relation between the volume averages of the micro-strains $\langle \boldsymbol{\varepsilon}_{\mathrm{m}}(\boldsymbol{x})\rangle_{\omega}$ and micro-stresses $\langle \boldsymbol{\sigma}_{\mathrm{m}}(\boldsymbol{x})\rangle_{\omega}$ over the meso-scale volume element ω, with

$$\boldsymbol{\varepsilon}_{\mathrm{M}} = \langle \boldsymbol{\varepsilon}_{\mathrm{m}}(\boldsymbol{x})\rangle_{\omega} \quad \text{and} \quad \boldsymbol{\sigma}_{\mathrm{M}} = \langle \boldsymbol{\sigma}_{\mathrm{m}}(\boldsymbol{x})\rangle_{\omega}\,, \tag{15}$$

where $\langle f(\boldsymbol{x})\rangle_{\omega} = \frac{1}{V_{\omega}}\int_{\omega} f(\boldsymbol{x})\mathrm{d}V$ and V_{ω} is the volume of the meso-scale volume element ω. Considering a two-phase isothermal composite material, with the respective volume fractions $v_0 + v_{\mathrm{I}} = 1$ (subscript 0 refers to the matrix and I to the inclusions), Eq. (15) can be rewritten by separating the volume averages on the matrix subdomain ω_0 and on the inclusions subdomain ω_{I} as

$$\boldsymbol{\varepsilon}_{\mathrm{M}} = v_0\langle \boldsymbol{\varepsilon}_{\mathrm{m}}\rangle_{\omega_0} + v_{\mathrm{I}}\langle \boldsymbol{\varepsilon}_{\mathrm{m}}\rangle_{\omega_{\mathrm{I}}} \quad \text{and} \quad \boldsymbol{\sigma}_{\mathrm{M}} = v_0\langle \boldsymbol{\sigma}_{\mathrm{m}}\rangle_{\omega_0} + v_{\mathrm{I}}\langle \boldsymbol{\sigma}_{\mathrm{m}}\rangle_{\omega_{\mathrm{I}}}\,. \tag{16}$$

In what follows, the notations $\langle \bullet_{\mathrm{m}}\rangle_{\omega_i}$ are replaced by $\langle \bullet\rangle_i$ for conciseness.

4.1.1. Case of linear elasticity

For linear elastic phases, the relation between $\boldsymbol{\varepsilon}_{\mathrm{M}}$ and $\boldsymbol{\sigma}_{\mathrm{M}}$ can be evaluated from the set of Eqs. (16) completed with the constitutive laws of each phase, *i.e.* $\langle \boldsymbol{\sigma}\rangle_i = \mathbb{C}_i^{\mathrm{el}} : \langle \boldsymbol{\varepsilon}\rangle_i$ considering a uniform elasticity tensor $\mathbb{C}_i^{\mathrm{el}}$ for the phase ω_i, and with a relation linking the strain averages per phase such as

$$\langle \boldsymbol{\varepsilon}\rangle_{\mathrm{I}} = \mathbb{B}^{\epsilon}(\mathrm{I}, \mathbb{C}_0^{\mathrm{el}}, \mathbb{C}_{\mathrm{I}}^{\mathrm{el}}) : \langle \boldsymbol{\varepsilon}\rangle_0\,. \tag{17}$$

In this relation, $\mathbb{B}^{\epsilon}$ is the strain concentration tensor, which depends on (I), the geometrical information of the inclusion phase, and on the elasticity tensors of both phases. Considering the Mori-Tanaka (M-T) model [24], the strain concentration tensor reads

$$\mathbb{B}^{\epsilon}(\mathrm{I}, \mathbb{C}_0, \mathbb{C}_{\mathrm{I}}) = \{\mathbb{I} + \mathbb{S}(\mathrm{I}, \mathbb{C}_0) : [(\mathbb{C}_0)^{-1} : \mathbb{C}_{\mathrm{I}} - \mathbb{I}]\}^{-1}\,, \tag{18}$$

where $\mathbb{C}_0$ and $\mathbb{C}_\mathrm{I}$ are the considered phase linear operators, *i.e.* respectively $\mathbb{C}_0^\mathrm{el}$ and $\mathbb{C}_\mathrm{I}^\mathrm{el}$ in the context of linear elasticity, and where $\mathbb{S}(\mathrm{I}, \mathbb{C}_0)$ is the Eshelby tensor [23].

Finally, for linear elastic composites, the set of Eqs. (16-17) is rewritten in a general constitutive expression as

$$\boldsymbol{\sigma}_\mathrm{M} = \mathbb{C}_\mathrm{M}^\mathrm{el}(\mathrm{I}, \mathbb{C}_0^\mathrm{el}, \mathbb{C}_\mathrm{I}^\mathrm{el}, v_\mathrm{I}) : \boldsymbol{\varepsilon}_\mathrm{M} \,. \tag{19}$$

4.1.2. Definition of Linear Comparison Composite (LCC) and extension to non-linear behaviours

In a non-linear framework, the MFH is carried out in an incremental form from the configuration at time t_n to the configuration at time t_{n+1} through the definition of a so-called Linear Comparison Composite (LCC). The LCC is a virtual heterogeneous material, whose constituents linear behaviours, defined through virtual elastic operators, match the linearised behaviours of the real composite material constituents for a given stress-strain state. The MFH equations of the linear composite material can then be applied by considering the virtual elastic operators $\mathbb{C}_0^\mathrm{LCC}$ of the matrix phase and $\mathbb{C}_\mathrm{I}^\mathrm{LCC}$ of the inclusions phase. The set of Eqs. (16) is thus rewritten as

$$\Delta\boldsymbol{\varepsilon}_\mathrm{M} = v_0\langle\Delta\boldsymbol{\varepsilon}\rangle_0 + v_\mathrm{I}\langle\Delta\boldsymbol{\varepsilon}\rangle_\mathrm{I} \quad \text{and} \quad \boldsymbol{\sigma}_\mathrm{M} = v_0\langle\boldsymbol{\sigma}\rangle_0 + v_\mathrm{I}\langle\boldsymbol{\sigma}\rangle_\mathrm{I} \,, \tag{20}$$

with the relation between the averaged incremental strains in the two phases (17) becoming

$$\langle\Delta\boldsymbol{\varepsilon}\rangle_\mathrm{I} = \mathbb{B}^\epsilon(\mathrm{I}, \mathbb{C}_0^\mathrm{LCC}, \mathbb{C}_\mathrm{I}^\mathrm{LCC}) : \langle\Delta\boldsymbol{\varepsilon}\rangle_0 \,. \tag{21}$$

Different linearisation approaches were developed in order to define the LCC. The secant formulation [53] considers, for each phase, the secant operator defined from the total strain and the total stress, *i.e.* $\langle\boldsymbol{\sigma}\rangle_i = \mathbb{C}_i^\mathrm{sec} : \langle\boldsymbol{\varepsilon}\rangle_i$. This method is however limited to monotonic and proportional loading conditions. In order to account for non-monotonic loading conditions, the incremental-tangent approach is based on a rate formulation of the local problem [28, 54, 34, 55, 56]. During a strain increment, one has $\delta\langle\Delta\boldsymbol{\sigma}\rangle_i = \mathbb{C}_i^\mathrm{alg} : \delta\langle\Delta\boldsymbol{\varepsilon}\rangle_i$ in each phase, with the phases algorithmic operators $\mathbb{C}_i^\mathrm{alg}$ used to define the LCC. Still with the aim of capturing non-monotonic loading, a polarisation tensor $\boldsymbol{\tau}$ is introduced in the affine method [57, 58, 59, 35, 60], yielding $\langle\boldsymbol{\sigma}\rangle_i = \mathbb{C}_i : \langle\boldsymbol{\varepsilon}\rangle_i + \boldsymbol{\tau}_i$, in which case $\mathbb{C}_i$ can be different from the tangent moduli. Nevertheless both the incremental-tangent and the affine methods suffer from some limitations: i) they require an isotropic projection of the tangent operators in the homogenization process in order to prevent over-stiff estimates [61]; ii) they can lead to poor accuracy in the case of non-proportional loading [37]; and iii) they cannot handle damage in a phase beyond the strain softening onset since they are unable to model the potential elastic unloading arising in the other phase [39]. These limitations have motivated the development of the incremental-secant formulation, which considers the secant form $\langle\Delta\boldsymbol{\sigma}\rangle_i^r = \mathbb{C}_i^\mathrm{S} : \langle\Delta\boldsymbol{\varepsilon}\rangle_i^r$ applied from a virtually unloaded state as described in the next Section 4.2. For completeness, second statistical moment values in the different phases can also be considered in the

different cited MFH formulations [62, 63, 64, 65] or used in combination with the first order moment values [66, 67]. Besides, variational formulations [32] were shown to be equivalent to the second-order secant formulation [62], whilst non-proportional loading can be handled with incremental variational formulations [68, 69, 70, 71, 72, 73].

These equations are completed by the constitutive behaviour models of the phases. The average stress at configuration time t_{n+1} in the phase ω_i results from the constitutive box

$$\langle \boldsymbol{\sigma} \rangle_i (t_{n+1}) = \boldsymbol{\sigma} \left(\langle \boldsymbol{\varepsilon} \rangle_i (t_{n+1}) , \tilde{\mathbf{Z}}_i (\tau) ; \mathbf{Z}_i (\tau) , \tau \in [0, t] \right) , \tag{22}$$

where $\mathbf{Z}_i$ is a set of internal variables used to account for history-dependent behaviours. Furthermore, anticipating on the case in which a damaging process is considered in a non-local form, a subset of the internal variables $\mathbf{Z}_i$ is associated to a set of non-local internal variables denoted as $\tilde{\mathbf{Z}}_i$ which are kinematics variables arising from the finite element resolution of an auxiliary field, as it will be further detailed.

4.2. Incremental-secant MFH with damage model in both phases

Among the possible different linearisation techniques developed in order to define the LCC, the incremental-secant method considers a virtual unloading step of the composite material followed by a secant loading from the residual states reached in both phases. This secant loading is used to define the virtual elastic operators $\mathbb{C}_0^{\mathrm{LCC}}$ and $\mathbb{C}_{\mathrm{I}}^{\mathrm{LCC}}$. This approach has been shown to exhibit a good accuracy in the case of non-proportional loading [37] and in the case of damage-enhanced elasto-plasticity since it allows capturing a phase elastic unloading during softening of another one [39]. Details on the incremental-secant approach can be found in the references [37, 39], while it is herein extended to account for the damaging process in the fibre bundles using the model developed in Section 2.

4.2.1. Virtual elastic unloading

The virtual elastic unloading is conducted on the composite material from the configuration at time t_n to reach a residual state so that $\boldsymbol{\sigma}_{\mathrm{M}\,n}^{\mathrm{res}} = 0$, where the superscript "res" refers to the virtually unloaded state. The case of damage-enhanced elasto-plasticity is illustrated in Figs. 4(a) and 4(b) for respectively the composite material and the phase ω_i. Since this virtual unloading is elastic, the LCC is defined from the phase damaged elastic operators, that are particularised in Section 4.3 for $\mathbb{C}_0^{\mathrm{el\,D}}$, the damaged elastic operator of the matrix phase ω_0, and in Section 4.4 for $\mathbb{C}_{\mathrm{I}}^{\mathrm{el\,D}}$, the damaged elastic operator of the fibre bundle phase ω_{I}. This yields the strain concentration tensor, see Eq. (21), which reads $\mathbb{B}^{\epsilon}(\mathrm{I}, \mathbb{C}_0^{\mathrm{el\,D}}, \mathbb{C}_{\mathrm{I}}^{\mathrm{el\,D}})$. We note that during this virtual unloading step the damaged elastic operators are constant since elasticity is assumed at constant damage variables.

The unloading can be solved analytically using Eq. (19) rewritten as

$$\boldsymbol{\sigma}_{\mathrm{M}n} = \mathbb{C}_{\mathrm{M}}^{\mathrm{el\,D}}(\mathrm{I}, \mathbb{C}_0^{\mathrm{el\,D}}, \mathbb{C}_{\mathrm{I}}^{\mathrm{el\,D}}, v_{\mathrm{I}}) : \Delta\boldsymbol{\varepsilon}_{\mathrm{M}}^{\mathrm{unload}} , \tag{23}$$

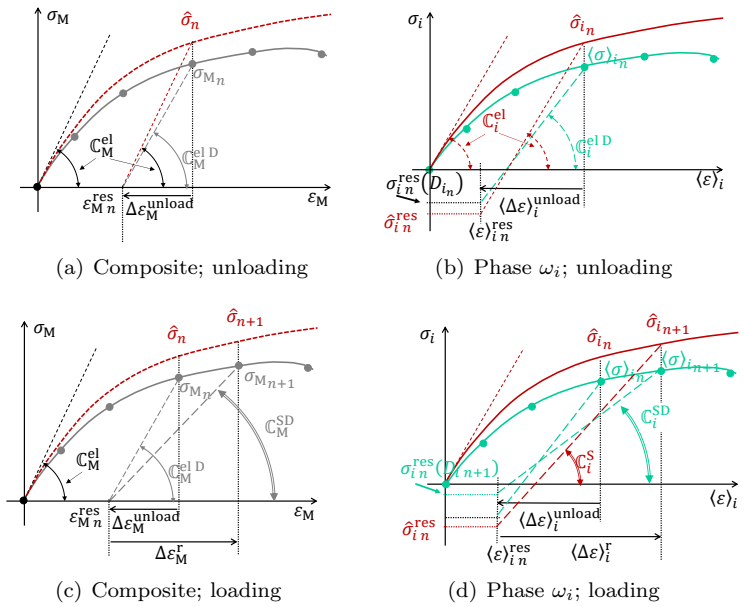

(a) Composite; unloading (b) Phase ω_i; unloading

(c) Composite; loading (d) Phase ω_i; loading

Figure 4: Definition of the LCC in the incremental-secant method for damage-enhanced elasto-plastic composites: (a) Virtual elastic unloading of the composite material with the elastic operator $\mathbb{C}_{\mathrm{M}}^{\mathrm{el\,D}}$, the red dotted line corresponds to an undamaged composite material and is shown for illustration purpose only; (b) Corresponding virtual elastic unloading of an elasto-plastic phase ω_i with the elastic operator $\mathbb{C}_i^{\mathrm{el\,D}}$, the red line corresponds to the effective stress-strain curve (or undamaged phase material); (c) Incremental-secant loading of the composite material from the virtually unloaded state and definition of the incremental-secant operator $\mathbb{C}_{\mathrm{M}}^{\mathrm{S\,D}}$; and (d) Corresponding incremental-secant loading of a damage-enhanced elasto-plastic phase ω_i from the residual undamaged stress and definition of the incremental-secant phase operator $\mathbb{C}_i^{\mathrm{S}}$; the damaged incremental-secant phase operator $\mathbb{C}_i^{\mathrm{S\,D}}$ is obtained in the apparent stress space.

where the macro-scale damaged elastic operator $\mathbb{C}_{\mathrm{M}}^{\mathrm{el\,D}}$ reads

$$\begin{aligned}\mathbb{C}_{\mathrm{M}}^{\mathrm{el\,D}} \;=\; & \left[v_{\mathrm{I}}\mathbb{C}_{\mathrm{I}}^{\mathrm{el\,D}} : \mathbb{B}^{\epsilon}(\mathrm{I}, \mathbb{C}_0^{\mathrm{el\,D}}, \mathbb{C}_{\mathrm{I}}^{\mathrm{el\,D}}) + v_0\mathbb{C}_0^{\mathrm{el\,D}}\right] : \\ & \left[v_{\mathrm{I}}\mathbb{B}^{\epsilon}(\mathrm{I}, \mathbb{C}_0^{\mathrm{el\,D}}, \mathbb{C}_{\mathrm{I}}^{\mathrm{el\,D}}) + v_0\mathbb{I}\right]^{-1} . \end{aligned} \tag{24}$$

Although the residual stress related to the unloaded composite material vanishes, *i.e.* $\boldsymbol{\sigma}_{\mathrm{M}}^{\mathrm{res}} = 0$, this is not the case for the different phases, see Fig. 4(b), which are characterised by a residual strain tensor $\langle\boldsymbol{\varepsilon}\rangle_{i_n}^{\mathrm{res}} = \langle\boldsymbol{\varepsilon}\rangle_{i_n} - \langle\Delta\boldsymbol{\varepsilon}\rangle_i^{\mathrm{unload}}$ and a residual stress tensor $\langle\boldsymbol{\sigma}\rangle_{i_n}^{\mathrm{res}}$ obtained from the resolution of the set of linear Eqs. (20-21) rewritten using the strain concentration tensor $\mathbb{B}^{\epsilon}(\mathrm{I}, \mathbb{C}_0^{\mathrm{el\,D}}, \mathbb{C}_{\mathrm{I}}^{\mathrm{el\,D}})$ and the macro-strain variation $\Delta\boldsymbol{\varepsilon}_{\mathrm{M}}^{\mathrm{unload}}$.

Since the virtual unloading was performed at constant damage value D_i in the phase ω_i, and since this damage variable will evolve during the loading increment from configuration at time t_n to configuration at time t_{n+1}, we use the notation $\boldsymbol{\sigma}_{i_n}^{\mathrm{res}}(D_{i_n})$ to define the apparent residual stress obtained after

unloading at configuration n for a damage variable D_i. We also report in Fig. 4 the effective stress-strain curves, where we have used the $\hat{\boldsymbol{\sigma}}$ notation to refer to the stress in the undamaged material classically defined when considering continuum damage mechanics. We note that the effective residual stress $\hat{\boldsymbol{\sigma}}^{\mathrm{res}}_{i_n}$ does not depend on the variable D_i but the apparent residual stress $\boldsymbol{\sigma}^{\mathrm{res}}_{i_n}$ does. Since the residual stress states are not strictly volume averages, we do not use the $\langle\bullet\rangle$ notation.

4.2.2. Incremental-secant loading

The secant linearisation of the non-linear composite material is carried out in the time interval $[t_n,\, t_{n+1}]$ from the residual state with the strain increment $\Delta\boldsymbol{\varepsilon}^{\mathrm{r}}_{\mathrm{M}}$ defined such that

$$\boldsymbol{\varepsilon}_{\mathrm{M}_{n+1}} = \boldsymbol{\varepsilon}^{\mathrm{res}}_{\mathrm{M}_n} + \Delta\boldsymbol{\varepsilon}^{\mathrm{r}}_{\mathrm{M}}\,, \tag{25}$$

see Fig. 4(c), where $\boldsymbol{\varepsilon}_{\mathrm{M}_{n+1}}$ is known from the macro-scale BVP. The phase strain increments $\langle\Delta\boldsymbol{\varepsilon}\rangle^{\mathrm{r}}_i$ are defined from the phase residual strains reached upon unloading such that

$$\langle\boldsymbol{\varepsilon}\rangle_{i_{n+1}} = \langle\boldsymbol{\varepsilon}\rangle^{\mathrm{res}}_{i_n} + \langle\Delta\boldsymbol{\varepsilon}\rangle^{\mathrm{r}}_i\,, \tag{26}$$

as illustrated in Fig. 4(d).

The average stress at configuration time t_{n+1} in the phase ω_i results from the constitutive box (22), allowing to write the apparent stress increment in the phase ω_i from the unloaded configuration as

$$\langle\boldsymbol{\sigma}\rangle_{i_{n+1}} - \boldsymbol{\sigma}^{\mathrm{res}}_{i_n}\left(D_{i_{n+1}}\right) = \mathbb{C}^{\mathrm{S\,D}}_i : \langle\Delta\boldsymbol{\varepsilon}\rangle^{\mathrm{r}}_i\,, \tag{27}$$

with $\boldsymbol{\sigma}^{\mathrm{res}}_{i_n}\left(D_{i_{n+1}}\right)$ defining the apparent residual stress that would be reached at configuration t_n with the damage variable reached at configuration t_{n+1}, see Fig. 4(d). Eq. (27) defines the incremental-secant operator $\mathbb{C}^{\mathrm{S\,D}}_i$ of the damaged phase ω_i.

Therefore, the LCC is defined from the phase residual states using the incremental-secant operators $\mathbb{C}^{\mathrm{S\,D}}_i$, which yield the strain concentration tensor $\mathbb{B}^{\epsilon}(\mathrm{I}, \mathbb{C}^{\mathrm{S\,D}}_0, \mathbb{C}^{\mathrm{S\,D}}_{\mathrm{I}})$, see Eq. (21), which reads. The set of Eqs. (20-21) is thus rewritten in terms of the strain increments $\Delta\boldsymbol{\varepsilon}^{\mathrm{r}}_{\mathrm{M}}$, $\langle\Delta\boldsymbol{\varepsilon}\rangle^{\mathrm{r}}_i$, and of the strain concentration tensor $\mathbb{B}^{\epsilon}(\mathrm{I}, \mathbb{C}^{\mathrm{S\,D}}_0, \mathbb{C}^{\mathrm{S\,D}}_{\mathrm{I}})$. The resolution of this set of non-linear MFH equations follows an iterative process detailed in [39].

The expressions of the damaged incremental-secant operators $\mathbb{C}^{\mathrm{S\,D}}_i$ are now specified for both phases.

4.3. Matrix non-local damage model

The detailed expressions of the incremental-secant operators for the non-local formulation of a damage-enhanced elasto-plastic material can be found in [39, 21] and are hereafter summarised.

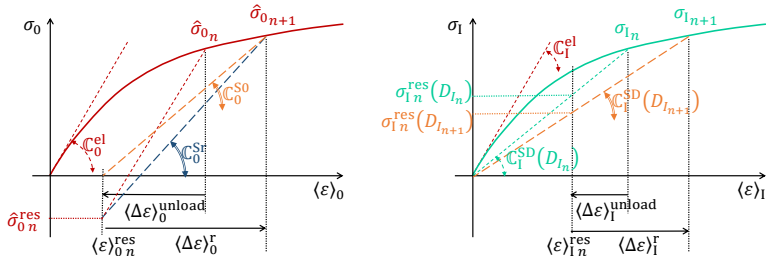

(a) Phase ω_0 (b) Phase ω_I

Figure 5: Particularisation of the LCC in the incremental-secant method for a (a) Damage-enhanced elasto-plastic matrix, with the definition in the effective stress space of the incremental-secant phase operator $\mathbb{C}_0^{Sr}$ from the residual stress and of the incremental-secant phase operator $\mathbb{C}_0^{S0}$ from the zero-stress state; and for a (b) Damage-enhanced elastic fibre bundle.

4.3.1. Non-local damage model

The constitutive Eq. (22) is first detailed in the case of elasto-plastic materials enhanced by a non-local damage model. In this section, for conciseness, we omit the subscript $n+1$ to refer to the configuration t_{n+1} as well as the subscript "0" and the average operator "$\langle\bullet\rangle$" used to refer to the volume average on the matrix phase.

Considering the strain equivalence assumption for which the strain tensors observed in the actual body and in its undamaged or effective representation are equivalent [74], the effective or undamaged stress $\hat{\boldsymbol{\sigma}}$ is defined from the apparent stress $\boldsymbol{\sigma}$ by introducing a damage parameter $0 \leq D < 1$, such that

$$\hat{\boldsymbol{\sigma}} = \frac{\boldsymbol{\sigma}}{(1-D)}\,. \tag{28}$$

Assuming a J_2 elasto-plastic material, and assuming that the plastic flow equations can be written in the effective stress space, the von Mises stress criterion reads

$$f = \hat{\sigma}^{\mathrm{eq}} - R(p) - \sigma_Y \leqslant 0\,, \tag{29}$$

where f is the yield surface, $\hat{\sigma}^{\mathrm{eq}} = \sqrt{\frac{3}{2}\frac{\mathrm{dev}(\boldsymbol{\sigma})}{1-D} : \frac{\mathrm{dev}(\boldsymbol{\sigma})}{1-D}}$ is the equivalent von Mises effective stress, σ_Y is the initial yield stress, $R(p) \geqslant 0$ is the isotropic hardening stress, and p is the internal variable characterising the irreversible behaviour, here the equivalent plastic strain[2]. Satisfying Eq. (29) and the plastic flow rule, see Appendix A.1, defines the set of internal variables $\mathbf{Z} = \{p, \boldsymbol{\varepsilon}^{\mathrm{pl}}\}$, with $\boldsymbol{\varepsilon}^{\mathrm{pl}}$ the plastic strain tensor.

[2]Rigorously, the von Mises stress criterion (29) should be written $f(\hat{\boldsymbol{\sigma}}, r) \leqslant 0$, where r is an internal variable related to the accumulated plastic strain p and to the plastic multiplier $\dot{\lambda}$ following $\dot{r} = \dot{\lambda} = (1-D)\dot{p}$, see the discussion by [76] for details.

The damage evolution is formulated in a non-local constitutive equation in order to avoid mesh-dependency upon strain localisation:

$$\begin{cases} \dot{D}\left(t\right) = \mathcal{D}\left(D\left(t\right), \boldsymbol{\varepsilon}\left(t\right), \chi(t); \mathbf{Z}\left(\tau\right), \tau \in [0, t]\right) \dot{\chi}\,, \\ \chi(t) = \max_{\tau \in [0,\, t]} \left(p_C, \tilde{p}\left(\tau\right)\right) \end{cases} \tag{30}$$

where χ is the maximum of the damage threshold p_C and of the maximum non-local internal variable $\tilde{p}$ reached during the process. The set of non-local internal variables $\tilde{\mathbf{Z}}$ is thus the scalar $\{\tilde{p}\}$, which is evaluated using the implicit non-local model [40, 77, 78]. The implicit non-local framework defines the relation between an internal variable $p \in \mathbf{Z}$ to its non-local counterpart $\tilde{p} \in \tilde{\mathbf{Z}}$ as an Helmholtz-type equation

$$\tilde{p} - \nabla \cdot \boldsymbol{c}_{\mathrm{g}} \cdot \nabla \tilde{p} = p\,, \tag{31}$$

where $\boldsymbol{c}_{\mathrm{g}}$ is the matrix of the squared characteristic lengths that have been introduced in [21] to account for material anisotropy. Indeed, when embedded in the MFH, this non-local formulation allows defining a longer non-local length along the UD-fibre direction so that the fibres "block" the matrix material-point interactions in the transverse directions of UD-fibre, and on the contrary, "prolong" the interaction in the longitudinal direction.

The stress $\boldsymbol{\sigma}\left(\boldsymbol{\varepsilon},\, D(p,\, \boldsymbol{\varepsilon}^{\mathrm{pl}};\, \tilde{p});\, p,\, \boldsymbol{\varepsilon}^{\mathrm{pl}}\right)$ thus follows, see Appendix A.1.

In this work, the evolution of the damage (30) is obtained from a saturated damage evolution, yielding

$$D = \frac{D_{\max}}{1 - \frac{1}{1+\exp\left(sp_{\mathrm{C}}\right)}} \left(\frac{1}{1+\exp\left(-s(\chi - p_{\mathrm{C}})\right)} - \frac{1}{1+\exp\left(sp_{\mathrm{C}}\right)} \right)\,, \tag{32}$$

where $D_{\max}$ is the saturation damage and s, p_{C} are two material parameters.

4.3.2. Damaged elastic material operator of the matrix material

The fourth-order Hooke tensor of the undamaged material reads

$$\mathbb{C}_0^{\mathrm{el}} = 3\kappa_0 \mathbb{I}^{\mathrm{vol}} + 2\mu_0 \mathbb{I}^{\mathrm{dev}}\,, \tag{33}$$

with κ_0 and μ_0 the elastic bulk and shear modulii of the undamaged material and with the spherical and deviatoric operators $\mathbb{I}^{\mathrm{vol}} = \frac{1}{3}\boldsymbol{I} \otimes \boldsymbol{I}$ and $\mathbb{I}^{\mathrm{dev}} = \mathbb{I} - \mathbb{I}^{\mathrm{vol}}$. Using the relation (28), the phase damaged fourth-order elastic operator $\mathbb{C}_0^{\mathrm{el\,D}}$ can directly be evaluated as $(1 - D_0)\mathbb{C}_0^{\mathrm{el}}$ from Eq. (33) as

$$\mathbb{C}_0^{\mathrm{el\,D}}(D_0) = 3(1 - D_0)\kappa_0 \mathbb{I}^{\mathrm{vol}} + 2(1 - D_0)\mu_0 \mathbb{I}^{\mathrm{dev}}\,. \tag{34}$$

4.3.3. Incremental-secant operators of the damage-enhanced elasto-plastic matrix material

Following Eq. (28), the residual stress reached upon virtual elastic unloading reads $\boldsymbol{\sigma}_{0_n}^{\mathrm{res}}\left(D_{0_n}\right) = \left(1 - D_{0_n}\right)\hat{\boldsymbol{\sigma}}_{0_n}^{\mathrm{res}}$ in the apparent stress state with $\hat{\boldsymbol{\sigma}}_{0_n}^{\mathrm{res}}$ the

residual stress in the effective stress state, see Fig. 4(b). The incremental loading, see Fig. 4(d), written in the effective stress space reads

$$\hat{\boldsymbol{\sigma}}_{0_{n+1}} - \hat{\boldsymbol{\sigma}}^{\mathrm{res}}_{0_n} = \mathbb{C}^{\mathrm{Sr}}_0 : \langle \Delta\boldsymbol{\varepsilon} \rangle^{\mathrm{r}}_0 \,. \tag{35}$$

The incremental-secant operator $\mathbb{C}^{\mathrm{Sr}}_0$ is naturally isotropic when considering the normal to the plastic flow from the residual state [37, 39], see Appendix A.1, in wich case the incremental-secant operator $\mathbb{C}^{\mathrm{Sr}}_0$ is written as

$$\mathbb{C}^{\mathrm{Sr}}_0 = 3\kappa_0 \mathbb{I}^{\mathrm{vol}} + 2\mu^{\mathrm{Sr}}_0 \mathbb{I}^{\mathrm{dev}} \,, \tag{36}$$

where κ_0 is the elastic bulk modulus of the undamaged matrix material and μ^{Sr}_0 is the secant shear modulus which reads

$$\mu^{\mathrm{Sr}}_0 = \frac{1}{3} \frac{\sqrt{\frac{3}{2}\mathrm{dev}\left(\hat{\boldsymbol{\sigma}}_{0_{n+1}} - \hat{\boldsymbol{\sigma}}^{\mathrm{res}}_{0_n}\right) : \mathrm{dev}\left(\hat{\boldsymbol{\sigma}}_{0_{n+1}} - \hat{\boldsymbol{\sigma}}^{\mathrm{res}}_{0_n}\right)}}{\sqrt{\frac{2}{3}\mathrm{dev}\left(\langle \Delta\boldsymbol{\varepsilon} \rangle^{\mathrm{r}}_0\right) : \mathrm{dev}\left(\langle \Delta\boldsymbol{\varepsilon} \rangle^{\mathrm{r}}_0\right)}} \,. \tag{37}$$

However, when considering first statistical moments only, it has been shown that the predictive capabilities of the incremental-secant method are improved in the case of hard inclusions when the residual stress in the matrix phase $\hat{\boldsymbol{\sigma}}^{\mathrm{res}}_{0_n}$ is cancelled when defining the incremental secant operator of the LCC [37, 65], see Fig. 5(a). Since for the studied material, the inclusion phase is stiffer than the matrix phase –even for highly damage fibre bundle, since the matrix also exhibits damage the damaged elasticity modulus of the fibre remains higher– so that we remove the residual of the matrix phase in Eq. (35), which becomes

$$\hat{\boldsymbol{\sigma}}_{0_{n+1}} = \mathbb{C}^{\mathrm{S0}}_0 : \langle \Delta\boldsymbol{\varepsilon} \rangle^{\mathrm{r}}_0 \,, \tag{38}$$

with

$$\mathbb{C}^{\mathrm{S0}}_0 = 3\kappa_0 \mathbb{I}^{\mathrm{vol}} + 2\mu^{\mathrm{S0}}_0 \mathbb{I}^{\mathrm{dev}} \,, \tag{39}$$

and with the increment shear modulus (37) rewritten as

$$\mu^{\mathrm{S0}}_0 = \frac{1}{3} \frac{\sqrt{\frac{3}{2}\mathrm{dev}\left(\hat{\boldsymbol{\sigma}}_{0_{n+1}}\right) : \mathrm{dev}\left(\hat{\boldsymbol{\sigma}}_{0_{n+1}}\right)}}{\sqrt{\frac{2}{3}\mathrm{dev}\left(\langle \Delta\boldsymbol{\varepsilon} \rangle^{\mathrm{r}}_0\right) : \mathrm{dev}\left(\langle \Delta\boldsymbol{\varepsilon} \rangle^{\mathrm{r}}_0\right)}} \,. \tag{40}$$

As a way of unifing the notations, the incremental secant operator is defined as

$$\mathbb{C}^{\mathrm{S}}_0 = 3\kappa_0 \mathbb{I}^{\mathrm{vol}} + 2\mu^{\mathrm{S}}_0 \mathbb{I}^{\mathrm{dev}} \,, \tag{41}$$

with μ^{S}_0 computed from either (37) or (40) depending whether the residual is kept or not in the matrix phase.

The incremental-secant damaged operator $\mathbb{C}^{\mathrm{S\,D}}_0$ is defined in the apparent stress space through Eq. (27). Since $\boldsymbol{\sigma}^{\mathrm{res}}_{0_n}\left(D_{0_{n+1}}\right) = \left(1 - D_{0_{n+1}}\right)\hat{\boldsymbol{\sigma}}^{\mathrm{res}}_{0_n}$, using Eq. (28) and Eq. (35), Eq. (27) yields

$$\mathbb{C}^{\mathrm{S\,D}}_0 : \langle \Delta\boldsymbol{\varepsilon} \rangle^{\mathrm{r}}_0 = \left(1 - D_{0_{n+1}}\right)\left[\hat{\boldsymbol{\sigma}}_{0_{n+1}} - \hat{\boldsymbol{\sigma}}^{\mathrm{res}}_{0_n}\right] = (1 - D_{0_{n+1}})\mathbb{C}^{\mathrm{S}}_0 : \langle \Delta\boldsymbol{\varepsilon} \rangle^{\mathrm{r}}_0 \,, \tag{42}$$

allowing defining the damaged incremental-secant operator

$$\mathbb{C}^{\mathrm{S\,D}}_0 = 3(1 - D_{0_{n+1}})\kappa_0 \mathbb{I}^{\mathrm{vol}} + 2(1 - D_{0_{n+1}})\mu^{\mathrm{S}}_0 \mathbb{I}^{\mathrm{dev}} = 3\kappa^{\mathrm{D}}_0 \mathbb{I}^{\mathrm{vol}} + 2\mu^{\mathrm{S\,D}}_0 \mathbb{I}^{\mathrm{dev}} \,, \tag{43}$$

with $\kappa^{\mathrm{D}}_0 = (1 - D_{0_{n+1}})\kappa_0$ and $\mu^{\mathrm{S\,D}}_0 = (1 - D_{0_{n+1}})\mu^{\mathrm{S}}_0$.

4.4. Embedded fibre bundle damage model

In this section, we embed the progressive damage model of the fibre bundle developed in Section 2.2 within the MFH scheme. The debonding of fibre-matrix interfaces near the fibre breaking point and the debonding caused by transverse loading on the composites are naturally captured by the damage evolution in the matrix phase.

4.4.1. Transverse isotropic elasticity

A transverse isotropic elastic model is used to describe the mechanical behaviour of the carbon fibres. The longitudinal direction of the fibres is refereed to by the superscript 3, and its two symmetric transverse directions by the superscripts 1 and 2. The elastic tensor of the transverse isotropic material is described by five independent elastic constants: the Young's modulus E_{I}^{1} and Poisson ratio $\nu_{\mathrm{I}}^{1\,2}$ in the transverse symmetry plane, the Young's modulus E_{I}^{3} and major Poisson ratio $\nu_{\mathrm{I}}^{3\,1}$ in the longitudinal direction, and the shear modulus $\mu_{\mathrm{I}}^{3\,1}$ in the longitudinal direction. These independent constants are completed by the definition of the minor Poisson coefficient $\nu_{\mathrm{I}}^{1\,3}$ with $\frac{\nu_{\mathrm{I}}^{1\,3}}{E_{\mathrm{I}}^{1}} = \frac{\nu_{\mathrm{I}}^{3\,1}}{E_{\mathrm{I}}^{3}}$, and the transverse shear modulus $\mu_{\mathrm{I}}^{1\,2}$ with $\mu_{\mathrm{I}}^{1\,2} = \frac{E_{\mathrm{I}}^{1}}{2(1+\nu_{\mathrm{I}}^{1\,2})}$.

In the local fibre axes, the expression of the transverse isotropic elastic tensor $\mathbf{C}_{\mathrm{I}}^{\mathrm{el}}$ reads in the Voigt notations

$$\mathbf{C}_{\mathrm{I}}^{\mathrm{el}} = \begin{bmatrix} \frac{E_{\mathrm{I}}^{1}(1-\nu_{\mathrm{I}}^{1\,3}\nu_{\mathrm{I}}^{3\,1})}{\Delta} & \frac{E_{\mathrm{I}}^{1}(\nu_{\mathrm{I}}^{1\,2}+\nu_{\mathrm{I}}^{1\,3}\nu_{\mathrm{I}}^{3\,1})}{\Delta} & \frac{E_{\mathrm{I}}^{1}(\nu_{\mathrm{I}}^{3\,1}+\nu_{\mathrm{I}}^{1\,2}\nu_{\mathrm{I}}^{3\,1})}{\Delta} & 0 & 0 & 0 \\ \frac{E_{\mathrm{I}}^{1}(\nu_{\mathrm{I}}^{1\,2}+\nu_{\mathrm{I}}^{1\,3}\nu_{\mathrm{I}}^{3\,1})}{\Delta} & \frac{E_{\mathrm{I}}^{1}(1-\nu_{\mathrm{I}}^{1\,3}\nu_{\mathrm{I}}^{3\,1})}{\Delta} & \frac{E_{\mathrm{I}}^{1}(\nu_{\mathrm{I}}^{3\,1}+\nu_{\mathrm{I}}^{1\,2}\nu_{\mathrm{I}}^{3\,1})}{\Delta} & 0 & 0 & 0 \\ \frac{E_{\mathrm{I}}^{3}(\nu_{\mathrm{I}}^{1\,3}+\nu_{\mathrm{I}}^{1\,2}\nu_{\mathrm{I}}^{1\,3})}{\Delta} & \frac{E_{\mathrm{I}}^{3}(\nu_{\mathrm{I}}^{1\,3}+\nu_{\mathrm{I}}^{1\,2}\nu_{\mathrm{I}}^{1\,3})}{\Delta} & \frac{E_{\mathrm{I}}^{3}(1-\nu_{\mathrm{I}}^{1\,2}\nu_{\mathrm{I}}^{1\,2})}{\Delta} & 0 & 0 & 0 \\ 0 & 0 & 0 & 2\mu_{\mathrm{I}}^{3\,1} & 0 & 0 \\ 0 & 0 & 0 & 0 & 2\mu_{\mathrm{I}}^{3\,1} & 0 \\ 0 & 0 & 0 & 0 & 0 & 2\mu_{\mathrm{I}}^{1\,2} \end{bmatrix}, \tag{44}$$

where $\Delta = (1+\nu_{\mathrm{I}}^{1\,2})(1-\nu_{\mathrm{I}}^{1\,2}-2\nu_{\mathrm{I}}^{1\,3}\nu_{\mathrm{I}}^{3\,1})$.

4.4.2. Local damage model

In this paper, the damage model of the fibre bundle is derived in a local form, and will require a further extension [80] to account for the energy resulting from the fibre breaking and debonding.

According to Section 2, and in particular Eqs. (1) and (9), the damage evolution of a fibre bundle in tension is summarised as

$$D_{\mathrm{I}} = \varphi + \varrho\sqrt{\frac{\varphi(1-\varphi)}{N}} \quad \text{with} \tag{45}$$

$$\varphi = 1.0 - \exp\left[-\left(\frac{L}{L_0}\right)^{\alpha}\left(\frac{\hat{\sigma}_{\mathrm{I}}^{3}}{\sigma_0}\right)^{m}\right], \tag{46}$$

where L, L_0, σ_0, m and α are material parameters, ϱ is a realisation of a random variable which follows a normal distribution $\mathcal{N}(0,1)$, N is the number of fibres considered, and where $\hat{\sigma}_{\mathrm{I}}^3$ represents the effective, or undamaged, longitudinal stress, which can be obtained from the relation $\hat{\boldsymbol{\sigma}}_{\mathrm{I}} = \mathbb{C}_{\mathrm{I}}^{\mathrm{el}} : \boldsymbol{\varepsilon}_{\mathrm{I}}$.

The apparent stress has now to be defined from the damage variable. Because of the anisotropy of the material, and because the fibre bundle damage does not affect the response of the bundle when embedded in a matrix the same way in all the directions, we do not consider a relation similar to Eq. (28). The idea in this section is to degrade the longitudinal behaviour under the constraints of transverse isotropy and of symmetry of the resulting damaged material operator. We thus affect the longitudinal Young's modulus following

$$E_{\mathrm{I}}^{3\,\mathrm{D}} = (1.0 - D_{\mathrm{I}})E_{\mathrm{I}}^3\,, \text{ and} \tag{47}$$

$$\nu_{\mathrm{I}}^{3\,1\,\mathrm{D}} = (1.0 - D_{\mathrm{I}})\nu_{\mathrm{I}}^{3\,1}\,, \tag{48}$$

where the second equation allows keeping $\frac{\nu_{\mathrm{I}}^{1\,3}}{E_{\mathrm{I}}^1}$ constant.

Because of the absence of plastic flow, we define the stress tensor as

$$\langle\boldsymbol{\sigma}\rangle_{\mathrm{I}} = \mathbb{C}_{\mathrm{I}}^{\mathrm{D}} : \langle\boldsymbol{\varepsilon}\rangle_{\mathrm{I}}\,, \tag{49}$$

yielding the damaged elasticity tensor, in the Voigt notations,

$$\mathbf{C}_{\mathrm{I}}^{\mathrm{D}}(D) = \begin{bmatrix} \frac{E_{\mathrm{I}}^1(1-\nu_{\mathrm{I}}^{1\,3}\nu_{\mathrm{I}}^{3\,1\,\mathrm{D}})}{\Delta^{\mathrm{D}}} & \frac{E_{\mathrm{I}}^1(\nu_{\mathrm{I}}^{1\,2}+\nu_{\mathrm{I}}^{1\,3}\nu_{\mathrm{I}}^{3\,1\,\mathrm{D}})}{\Delta^{\mathrm{D}}} & \frac{E_{\mathrm{I}}^1(\nu_{\mathrm{I}}^{3\,1\,\mathrm{D}}+\nu_{\mathrm{I}}^{1\,2}\nu_{\mathrm{I}}^{3\,1\,\mathrm{D}})}{\Delta^{\mathrm{D}}} & 0 & 0 & 0 \\ \frac{E_{\mathrm{I}}^1(\nu_{\mathrm{I}}^{1\,2}+\nu_{\mathrm{I}}^{1\,3}\nu_{\mathrm{I}}^{3\,1\,\mathrm{D}})}{\Delta^{\mathrm{D}}} & \frac{E_{\mathrm{I}}^1(1-\nu_{\mathrm{I}}^{1\,3}\nu_{\mathrm{I}}^{3\,1\,\mathrm{D}})}{\Delta^{\mathrm{D}}} & \frac{E_{\mathrm{I}}^1(\nu_{\mathrm{I}}^{3\,1\,\mathrm{D}}+\nu_{\mathrm{I}}^{1\,2}\nu_{\mathrm{I}}^{3\,1\,\mathrm{D}})}{\Delta^{\mathrm{D}}} & 0 & 0 & 0 \\ \frac{E_{\mathrm{I}}^{3\,\mathrm{D}}(\nu_{\mathrm{I}}^{1\,3}+\nu_{\mathrm{I}}^{1\,2}\nu_{\mathrm{I}}^{1\,3})}{\Delta^{\mathrm{D}}} & \frac{E_{\mathrm{I}}^{3\,\mathrm{D}}(\nu_{\mathrm{I}}^{1\,3}+\nu_{\mathrm{I}}^{1\,2}\nu_{\mathrm{I}}^{1\,3})}{\Delta^{\mathrm{D}}} & \frac{E_{\mathrm{I}}^{3\,\mathrm{D}}(1-\nu_{\mathrm{I}}^{1\,2}\nu_{\mathrm{I}}^{1\,2})}{\Delta^{\mathrm{D}}} & 0 & 0 & 0 \\ 0 & 0 & 0 & 2\mu_{\mathrm{I}}^{3\,1} & 0 & 0 \\ 0 & 0 & 0 & 0 & 2\mu_{\mathrm{I}}^{3\,1} & 0 \\ 0 & 0 & 0 & 0 & 0 & 2\mu_{\mathrm{I}}^{1\,2} \end{bmatrix}, \tag{50}$$

where $\Delta^{\mathrm{D}} = (1+\nu_{\mathrm{I}}^{1\,2})(1-\nu_{\mathrm{I}}^{1\,2}-2\nu_{\mathrm{I}}^{1\,3}\nu_{\mathrm{I}}^{3\,1\,\mathrm{D}})$.

4.4.3. Damaged elastic material operator of the fibre bundle material

The fibre bundle damaged fourth-order elastic operator $\mathbb{C}_{\mathrm{I}}^{\mathrm{el\,D}}$ is directly evaluated from Eq. (50) as

$$\mathbb{C}_{\mathrm{I}}^{\mathrm{el\,D}}(D_{\mathrm{I}}) = \mathbb{C}_{\mathrm{I}}^{\mathrm{D}}(D_{\mathrm{I}})\,, \tag{51}$$

with $D_{\mathrm{I}} = D_{\mathrm{I}_n}$ during the elastic unloading at configuration t_n.

4.4.4. Incremental-secant operators of the damage-enhanced fibre bundle material

In the absence of plastic-flow in the fibre bundle, the fourth-order incremental-secant operator $\mathbb{C}_{\mathrm{I}}^{\mathrm{S\,D}}$ of the fibre bundle is defined through Eq. (27). Following

Eq. (49), we define the residual stress from the virtual elastic-unloading at configuration t_n for the two damage configurations as

$$\boldsymbol{\sigma}_{\mathrm{I}_n}^{\mathrm{res}}\left(D_{\mathrm{I}_n}\right)=\mathbb{C}_{\mathrm{I}}^{\mathrm{D}}(D_{\mathrm{I}_n}):\langle\boldsymbol{\varepsilon}\rangle_{\mathrm{I}_n}^{\mathrm{res}} \quad \text{and} \quad \boldsymbol{\sigma}_{\mathrm{I}_n}^{\mathrm{res}}\left(D_{\mathrm{I}_{n+1}}\right)=\mathbb{C}_{\mathrm{I}}^{\mathrm{D}}(D_{\mathrm{I}_{n+1}}):\langle\boldsymbol{\varepsilon}\rangle_{\mathrm{I}_n}^{\mathrm{res}}, \tag{52}$$

as illustrated in Fig. 5(b). As a result, Eq. (27) yields

$$\begin{aligned}\mathbb{C}_{\mathrm{I}}^{\mathrm{S\,D}}:\langle\Delta\boldsymbol{\varepsilon}\rangle_{\mathrm{I}}^{\mathrm{r}} &= \langle\boldsymbol{\sigma}\rangle_{\mathrm{I}_{n+1}}-\boldsymbol{\sigma}_{\mathrm{I}_n}^{\mathrm{res}}\left(D_{\mathrm{I}_{n+1}}\right)=\mathbb{C}_{\mathrm{I}}^{\mathrm{D}}\left(D_{\mathrm{I}_{n+1}}\right):\left[\langle\boldsymbol{\varepsilon}\rangle_{\mathrm{I}_{n+1}}-\langle\boldsymbol{\varepsilon}\rangle_{\mathrm{I}_n}^{\mathrm{res}}\right]\\ &= \mathbb{C}_{\mathrm{I}}^{\mathrm{D}}\left(D_{\mathrm{I}_{n+1}}\right):\langle\Delta\boldsymbol{\varepsilon}\rangle_{\mathrm{I}}^{\mathrm{r}},\end{aligned} \tag{53}$$

and

$$\mathbb{C}_{\mathrm{I}}^{\mathrm{S\,D}}(D_{\mathrm{I}})=\mathbb{C}_{\mathrm{I}}^{\mathrm{el\,D}}(D_{\mathrm{I}})=\mathbb{C}_{\mathrm{I}}^{\mathrm{D}}(D_{\mathrm{I}}), \tag{54}$$

where $D_{\mathrm{I}}=D_{\mathrm{I}_{n+1}}$ is the damage reached during the reloading to configuration t_{n+1} and is evaluated through Eqs. (45) and (46) with the longitudinal stress $\langle\sigma^3\rangle_{\mathrm{I}_{n+1}}$. This set of equations needs to be solved together with the MFH iteration process.

4.5. Finite element implementation

In this work the damage evolution in the matrix phase is governed by a non-local form while the damage in the fibre bundle is treated in a local way. Therefore, the finite element implementation involves the discretisations of the displacement field $\boldsymbol{u}$ and of the auxiliary field $\tilde{p}_0$, which define the degrees of freedom of the problem. The governing equations correspond to the finite element discretisation of the weak forms of the linear momentum equation $\boldsymbol{\nabla}\cdot\boldsymbol{\sigma}_{\mathrm{M}}=0$ and of the auxiliary Eq. (31), and are detailed in [21].

In this formalism, the MFH is seen as a constitutive model, whose inputs are the macro-strain tensors $\boldsymbol{\varepsilon}_{\mathrm{M}_{n+1}}$ and $\boldsymbol{\varepsilon}_{\mathrm{M}_n}$ at two successive configurations, the auxiliary variable $\tilde{p}_{0_{n+1}}$ and the internal variables $\mathbf{Z}_{i_n}$ at the previous configuration in both phases, and whose outputs are the homogenised stress tensor given by Eq. (20) right, and its linearisation. Since the MFH is implemented as an advanced material constitutive box, the resolution remains efficient as compared to other multi-scale methods.

The stress linearisation reads

$$\begin{aligned}\delta\boldsymbol{\sigma}_{\mathrm{M}} &= \left(v_{\mathrm{I}}\mathbb{C}_{\mathrm{I}}^{\varepsilon\varepsilon}:\frac{\partial\langle\boldsymbol{\varepsilon}\rangle_{\mathrm{I}}}{\partial\boldsymbol{\varepsilon}_{\mathrm{M}}}+v_0\mathbb{C}_0^{\varepsilon\varepsilon}:\frac{\partial\langle\boldsymbol{\varepsilon}\rangle_0}{\partial\boldsymbol{\varepsilon}_{\mathrm{M}}}\right):\delta\boldsymbol{\varepsilon}_{\mathrm{M}}+\\ &\quad\left(v_{\mathrm{I}}\mathbb{C}_{\mathrm{I}}^{\varepsilon\varepsilon}:\frac{\partial\langle\boldsymbol{\varepsilon}\rangle_{\mathrm{I}}}{\partial\tilde{p}_0}+v_0\mathbb{C}_0^{\varepsilon\varepsilon}:\frac{\partial\langle\boldsymbol{\varepsilon}\rangle_0}{\partial\tilde{p}_0}+v_0\boldsymbol{C}_0^{\varepsilon\tilde{p}}\right)\delta\tilde{p}_0,\end{aligned} \tag{55}$$

where the derivatives $\frac{\partial\langle\boldsymbol{\varepsilon}\rangle_{\mathrm{I}}}{\partial\boldsymbol{\varepsilon}_{\mathrm{M}}}$, $\frac{\partial\langle\boldsymbol{\varepsilon}\rangle_0}{\partial\boldsymbol{\varepsilon}_{\mathrm{M}}}$, $\frac{\partial\langle\boldsymbol{\varepsilon}\rangle_{\mathrm{I}}}{\partial\tilde{p}_0}$ and $\frac{\partial\langle\boldsymbol{\varepsilon}\rangle_0}{\partial\tilde{p}_0}$ are obtained from the MFH resolution, more details can be found in [38, 39], and where the different material operators $\mathbb{C}_0^{\varepsilon\varepsilon}=\frac{\mathrm{d}\langle\boldsymbol{\sigma}\rangle_0}{\mathrm{d}\langle\boldsymbol{\varepsilon}\rangle_0}$, $\boldsymbol{C}_0^{\varepsilon\tilde{p}}=\frac{\mathrm{d}\langle\boldsymbol{\sigma}\rangle_0}{\mathrm{d}\tilde{p}_0}$, and $\mathbb{C}_{\mathrm{I}}^{\varepsilon\varepsilon}=\frac{\mathrm{d}\langle\boldsymbol{\sigma}\rangle_{\mathrm{I}}}{\mathrm{d}\langle\boldsymbol{\varepsilon}\rangle_{\mathrm{I}}}$ are given in Appendix A. Since Eq. (31) is also integrated at the finite element level, the linearisation of p_0 should also be provided through $\boldsymbol{C}_0^{p\varepsilon}=\frac{\mathrm{d}p_0}{\mathrm{d}\langle\boldsymbol{\varepsilon}\rangle_0}$, $C_0^{p\tilde{p}}=\frac{\mathrm{d}p_0}{\mathrm{d}\tilde{p}_0}=0$ as detailed in Appendix A.

5. Applications of the extended MFH on UD fibre reinforced composites

In this section we apply the MFH model developed to account for matrix cracking and fibre bundle breaking. We first present the material properties of the considered Unidirectional AS4 carbon fibre reinforced 8552 epoxy material system before studying the failure of a single unidirectional ply loaded in the longitudinal direction. The MFH model is then applied to a notched laminate for which the local failure modes are compared to experimental CT observations reported in the literature.

5.1. Material properties

5.1.1. Carbon fibres

The AS4 UD-carbon fibre bundles follow a transversely isotropic linear elastic constitutive material model. The typical mechanical properties of high strength PAN based carbon fibres are presented in Table 2. Since AS4 carbon fibres have a reported longitudinal tensile elastic modulus of 231 GPa, the Weibull function parameters of AS4 carbon fibre presented in Table 1, are used in the fibre bundle damage model presented in Section 2.2.

Table 2: Material properties of the AS4 carbon fibres [79].

Property	Value
Long. Young's modulus E_{I}^{3} [GPa]	231.0
Trans. Young's modulus E_{I}^{1} [GPa]	12.99
Trans. Poisson ratio ν_{I}^{12} [-]	0.46
Long.-Trans. Poisson ratio ν_{I}^{31} [-]	0.3
Trans. shear modulus μ_{I}^{12} [GPa]	4.45
Long.-Trans. shear modulus μ_{I}^{31} [GPa]	11.3

5.1.2. Epoxy matrix material

The epoxy material behaviour is modelled by the non-local damage formalism presented in Section 4.3.1, with the hardening law written in the effective stress space reading

$$R_0(p_0) = h_0 \left(1 - e^{-m_0 p_0}\right) , \tag{56}$$

where p_0 represents the matrix accumulated plastic strain of the matrix phase, and where h_0 and m_0 are two material parameters.

The elastic properties of cured 8552 epoxy are used. By lack of elasto-plastic data, the elasto-plastic parameters and damage parameters are evaluated in order to match the tensile strength of 121 MPa reported for 8552 epoxy. The matrix squared lengths tensor $\boldsymbol{c}_{\mathrm{g}}$, Eq. (31), is defined in order to represent the anisotropic nature of the matrix cracking in a UD ply. On the one hand, the transverse characteristic lengths $\sqrt{c^1} = \sqrt{c^2}$ can be tuned in order to recover

the critical energy release rate of transverse failure [49]. On the other hand, the longitudinal characteristic length $\sqrt{c^3}$ is taken large enough to promote matrix cracking along the fibre direction. The resulting material parameters are reported in Table 3, in which the characteristic length parameters of the non-local model are the values identified in reference [80] for the 8552 epoxy matrix.

Table 3: Material properties of the 8552 matrix.

Property	Value
Young's modulus E_0 [GPa]	4.668
Poisson ratio ν_0 [-]	0.39
Initial yield stress σ_{Y0} [MPa]	32.0
Hardening modulus h_0 [MPa]	300.0
Hardening exponent m_0 [-]	100.0
Saturated damage threshold $D_{\max_0}$ [-]	0.99
Saturated damage exponent s_0 [-]	700
Saturated damage plastic strain threshold p_{C0} [-]	0.007
Characteristic length c^1[mm^2]	25×10^{-4}
c^2[mm^2]	25×10^{-4}
c^3[mm^2]	2.0

5.1.3. Inter-laminar failure

In the case a laminate is considered, inter-laminar failure is modelled through extrinsic cohesive elements, see the details in [21]. The mixed-mode delamination law [81] is modified to take into account the effect of existing damage [21] and a potential is used to model the degradation, see Appendix B.

By lack of data for the AS4/8552 carbon-epoxy material system, the mode I and II critical energy release rates, $G_{\mathrm{I\,C}}$, $G_{\mathrm{II\,C}}$ and the critical stresses $\hat{\sigma}_{\mathrm{I\,C}}$, $\hat{\tau}_{\mathrm{II\,C}}$ are taken as the values used in the simulation of IM7/8552 carbon-epoxy composite laminates in Ref. [82] since it is assumed that the matrix properties are the most relevant to be considered. We however reduce the critical stress to 25 [MPa] to account for the finite size of the elements, see the discussion in [21]. The delamination model parameters are listed in Table 4.

Table 4: Material properties of the delamination model.

Property	Value
Mode I critical energy release rate $G_{\mathrm{I\,C}}$ [J/m^2]	277.0
Mode II critical energy release rate $G_{\mathrm{II\,C}}$ [J/m^2]	788.0
Mode I critical stress $\hat{\sigma}_{\mathrm{I\,C}}$ [MPa]	25
Mode II critical stress $\hat{\tau}_{\mathrm{II\,C}}$ [MPa]	25
Mixed mode parameter α [-]	1.0

5.2. *Predictions for the longitudinal tensile response of UD fibre reinforced composites*

In this section we discuss the response of a Unidirectional AS4 carbon fibre reinforced 8552 epoxy material system predicted by the MFH model developed to account for matrix cracking and fibre bundle breaking in Section 4. First the response of a material point is directly obtained for the longitudinal tension case from the MFH material law, and then the finite element discretisation of a ply is considered.

We consider as material properties of the Unidirectional AS4 carbon fibre reinforced 8552 epoxy the ones reported in Section 5.1. According to the discussion in Section 3, the length gauge parameter $L = 0.6$ mm is adopted for the Weibull distribution model of fibre damage. A nominal fibre volume fraction of $v_{\mathrm{I}} = 0.5742$ is reported for the AS4/8552 UD composites pre-preg [83]. Because of the chemical shrinkage of epoxy and the possible leakage during the curing process, the real fibre volume fraction in cured composites is always higher than that in their pre-preg. Unless otherwise stated, we consider a nominal fibre volume fraction $v_{\mathrm{I}} = 0.6$ for AS4/8552 UD composites.

5.2.1. *MFH predictions*

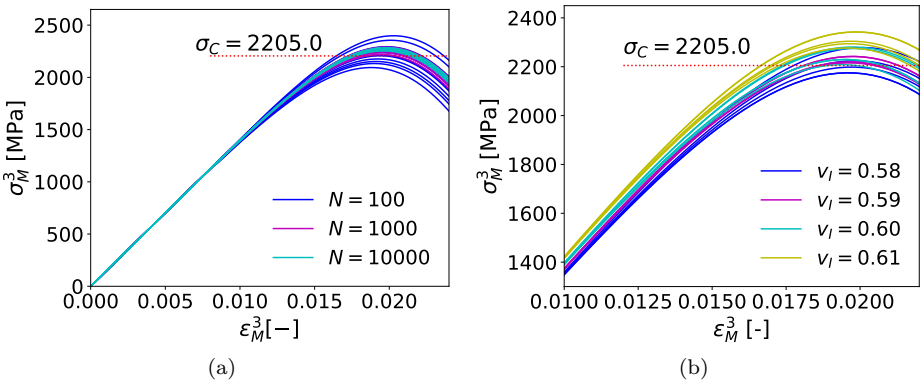

Figure 6: The strain-stress curves of longitudinal tensile tests of UD fibre reinforced composites with uncertainty enriched damage, (a) The effect of fibre number N on the discrepancy of the tensile response; (b) The effect of fibre volume fraction v_{I} on the tensile response, with $N = 1000$.

In this section, the MFH model is used to predict the mechanical response of UD fibre reinforced composites.

The uncertainty on the longitudinal tensile response of UD fibre reinforced composites, resulting from the damage evolution Eqs. (45) and (46), is studied by considering successively $N = 100$, 1000, and 10000 fibres by bundle. Considering a nominal fibre volume fraction $v_{\mathrm{I}} = 0.6$ for AS4/8552 UD composites, twelve simulations of unidirectional and longitudinal tension are performed for each fibres number and the predictions are reported in Fig. 6(a) for the different

values of N. The reported longitudinal tensile strength 2205 MPa of AS4/8552 UD composites [84] is also marked in Fig. 6(a). From Eq. (45), it can be seen that the uncertain damage evolution has a higher standard deviation for a lower value of N, which is also observed in Fig. 6(a) which shows that the discrepancy of the longitudinal tensile response decreases with the increase of fibres number N. The maximum tensile stress is reached for a damage of fibre bundle around $D_{\mathrm{I}} = 0.2$, the damage increasing abruptly to 1 beyond this value, see also Fig. 3. We note that the predicted tensile strength is rather close to the reported value in Ref. [84].

Since in practice the fibres are not uniformly distributed in the matrix and since the chemical shrinkage of epoxy is not uniform either in a cross-section, the fibre volume fraction is not uniform. This effect is now studied with $N = 1000$ fibres in the bundle by considering successively a volume fraction of $v_{\mathrm{I}} = 0.58$, 0.59, 0.60 and 0.61. Five simulations are performed for each fibre volume fraction in order to study the effect of v_{I} on the longitudinal tensile strength of UD fibre reinforced composites and, as it can be seen in Fig. 6(b), as expected, a higher fibre volume fraction leads to a higher longitudinal tensile strength on average.

5.2.2. MFH multi-scale finite element analysis

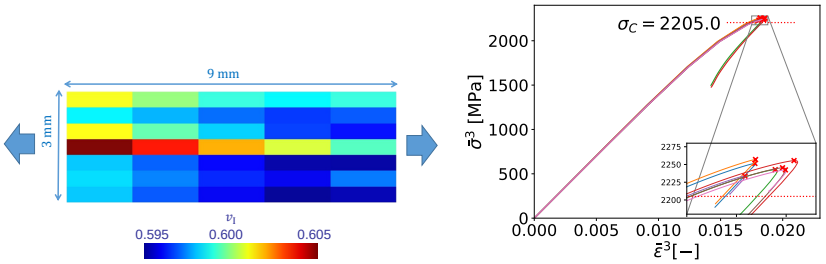

(a) (b)

Figure 7: Multi-scale finite element analysis of a longitudinal tensile test on a UD fibre reinforced epoxy: (a) Schematics of the ply and illustration of one realisation of the initial volume fraction distribution; and (b) Several apparent stress-strain curve realisations until reaching the failure point.

In this section, the multi-scale finite element analysis, with the MFH serving as constitutive law of the composites, is carried out on a composite ply tensile sample. The unidirectional tension simulation is performed along the longitudinal direction of the composites. The dimensions of the sample are 9.0×3.0 mm^2 and the latter is discretised with 1.8×0.429 mm^2 second order finite elements, see Fig. 7(a). The thickness of the sample is 0.25 mm. The element size is motivated by the fact that because of the existence of a size effect in the Weibull distribution of fibre strength, see Eq. (1), the longitudinal distance between integration points needs to be comparable with the length parameter L in order to represent the stochastic character of the failure point. However, if the geometry introduces a stress concentration, as it will be the case for the next test, the

failure point is then controlled by the stress concentration and the requirement of element size can be relaxed. The fibre volume fraction v_{I} is assumed to be a random variable, which does not account for any spatial correlation or size effect [85, 86] and which follows a Gaussian distribution $\mathcal{N}(0.60, 10^{-4})$, where 0.6 and 10^{-4} are respectively the mean value and variance of v_{I}. To be rigorous, the standard deviation should be related to the size of the finite element discretisation, but in the present application the uncertainty is introduced in order to trigger the failure. Since continuous fibres are considered, the fibre volume fraction v_{I} varies mainly along the transverse direction ($y-$ direction) of the composite ply and remains almost constant along the longitudinal direction ($x-$ direction), see Fig. 7(a). Considering a fibre radius $r = 3.5\,\mu$m, each Gaussian point represents the response of around 580 fibres and $N \approx 580$ is used in the simulation (the exact value is computed according to the value v_{I} associated to the Gauss point). Static resolution with a path-following method allowing for snapback is used to capture the failure point [87, 88].

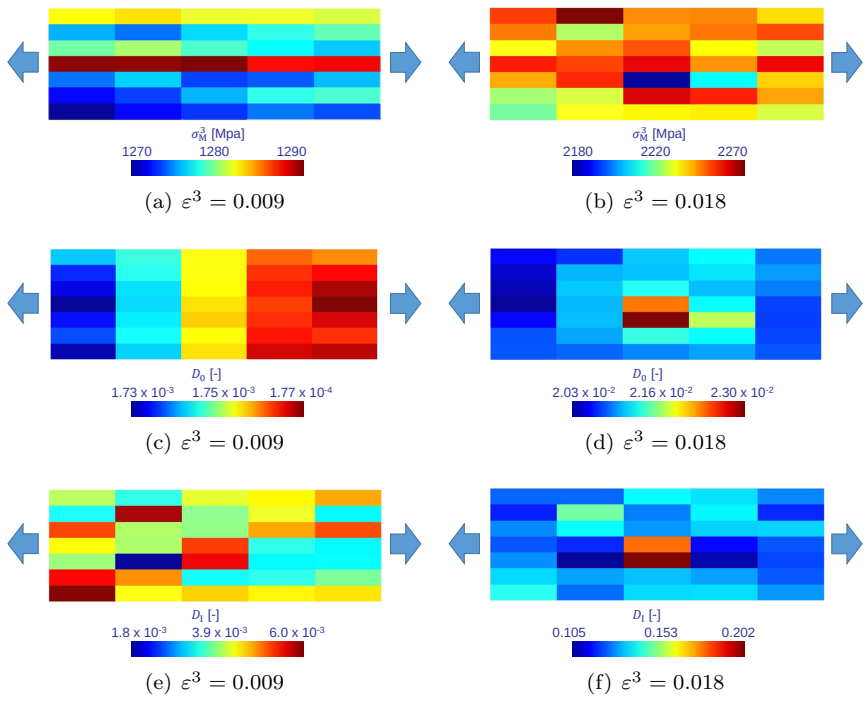

(a) $\varepsilon^3 = 0.009$ (b) $\varepsilon^3 = 0.018$

(c) $\varepsilon^3 = 0.009$ (d) $\varepsilon^3 = 0.018$

(e) $\varepsilon^3 = 0.009$ (f) $\varepsilon^3 = 0.018$

Figure 8: Fields distributions for one realisation of a multi-scale finite element analysis of a longitudinal tensile test on a UD fibre reinforced epoxy: (a, b) Longitudinal stress distribution at two different values of the ply strain; (c, d) Matrix damage distribution at two different values of the ply strain; and (e, f) Fibre bundle damage distribution at two different values of the ply strain; Averaged value on the quadratic finite elements are displayed.

The MFH multi-scale finite element analysis is carried out on eight realisations. The resulting stress-strain curves are reported in Fig. 7(b). From

Fig. 7(b), it can be seen that the predicted strengths are slightly above that of the reported value for AS4/8552 UD composites [84]. However, only a perfect geometry is considered in our simulations. Since only the size effect on the uncertainty of fibre strength is accounted for through the parameter N, and since the assumed distribution of the fibre volume fraction is not physically rigorous, the reduced discrepancy of the obtained longitudinal tensile strength is not reliable. In real experimental tests, the measured longitudinal tensile strength could have a much higher discrepancy because of the existence of other uncertainties, such as the variation in the fibre orientation, the existence of defects in the material, in the geometry and so on.

The longitudinal tensile stress σ^3, matrix damage D_0 and fibre bundle damage D_{I} distributions are illustrated at damage initiation and at failure in respectively Fig. 8(a), 8(c), 8(e) and Fig. 8(b), 8(d), 8(f) for a given realisation. Since the fibre volume fraction v_{I} has a larger variation along the transverse direction ($y-$ direction) as compared to the longitudinal direction ($x-$ direction), the longitudinal tensile stress σ^3 also displays a larger variation along the $y-$ direction before fibre bundle damage initiation, see Fig. 8(a). This pattern is however broken during damage evolution as illustrated in Fig. 8(b) at the failure point: in a given fibre bundle, the longitudinal stress at some locations becomes lower than at their neighbouring points one because of their higher damage values, see Fig. 8(f). Concerning the matrix damage distribution, comparing Figs. 8(c) and 8(e) at damage fibre initialisation with Figs. 8(d) and 8(f) at failure, it can be seen that the fibre bundle damage promotes the damage evolution in the matrix since a higher fibre bundle damage leads to a higher damage in the matrix.

5.3. Failure modes of a notched laminate

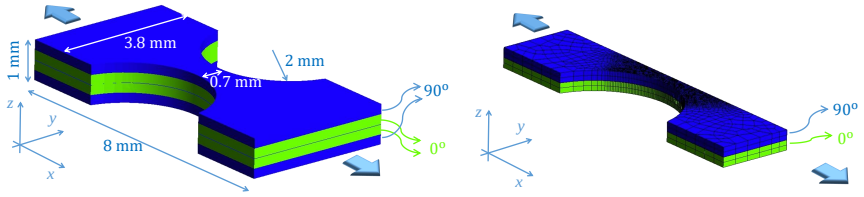

(a) (b)

Figure 9: MFH multi-scale finite element analysis of a double notched sample tensile test: (a) Dimensions and stacking sequence of the sample; and (b) Finite element discretisation of one quarter of the notched sample.

In this section, the multi-scale finite element analysis of a notched sample is carried out with the two-phase damage enhanced MFH, and the failure modes of the notched sample are compared with that of the experimental observations reported in Ref. [7]. The notched sample is cut from a UD fibre reinforce composite laminate and is subjected to a tensile test. The dimensions of the sample are given in Fig. 9(a), together with the layup of the laminate. According to the

symmetry of the sample, only one quarter is modelled using the multi-scale finite element framework. Its finite element discretisation is presented in Fig. 9(b). Quadratic hexahedral elements are considered with an element size, in the $x-y$ plane, of 40 μm at the notched part. The distance between integration points remains lower than the matrix non-local length. A dynamic implicit solver is used for this simulation. Since the matrix and fibre material properties used in our simulation are not exactly the same as for the material system used in Ref. [7], in which only the homogenised composites properties were presented, only a qualitative comparison between the simulation results and experimental study can be carried on. However, the two material systems consist in carbon fibre reinforced epoxy allowing to carry a comparison of the failure modes with the damage modes observed by Synchrotron radiation Computed Tomography (CT) in Ref. [7] and reported in Fig. 10 as a reference.

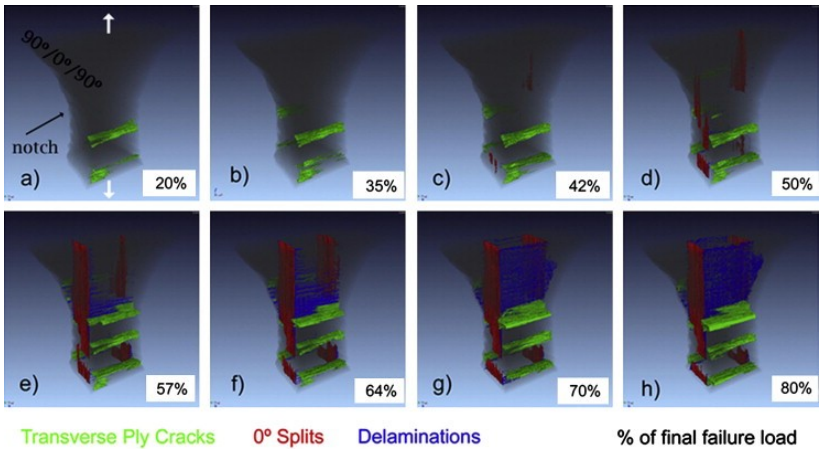

Figure 10: Experimental damage modes of the notched sample as observed in Ref. [7]. Reprinted from Composites Science and Technology, 71/12, A.E. Scott and M. Mavrogordato and P. Wright and I. Sinclair and S.M. Spearing, In situ fibre fracture measurement in carbonepoxy laminates using high resolution computed tomography, 1471-1477, Copyright (2011), with permission from Elsevier.

The predicted load-displacement curve is illustrated in Fig. 11. Because of the local damage formulation for the fibre bundle, the simulation is interrupted by lack of convergence when the fibre bundles start to enter locally in the softening. This motivates the development of a phase-field approach of the fibre bundle damaging process as conducted in [80]. We however estimate, from the strength of the 0°-ply studied in the previous Section 5.2.2, from the stacking sequence and from the presence of a stress concentration due to the notch that the laminate strength should be around 1000 MPa. We therefore compare the failure modes distribution at the configuration #1 and configuration #2 as reported in Fig. 11 to the CT images at 50% and 70% failure as reported in Fig. 10.

The stress and damage distributions at configuration #1 are illustrated in

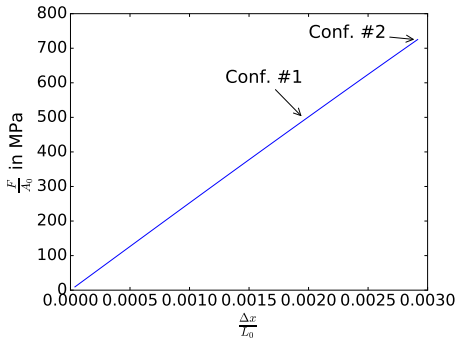

Figure 11: Numerical tensile load of the notched sample predicted by the MFH multi-scale finite element analysis.

Fig. 12. For the 0°-ply, the reached tensile stress, see Fig. 12(a), and the induced fibre bundle damage, see Fig. 12(g), are seen to localise at the notch. Shear stress distribution as illustrated in Fig. 12(c) is triggering the damage evolution in the matrix, see Fig. 12(e), which localises according to the so-called 0° splits as experimentally observed in Fig. 10(d). For the 90°-ply, the damage develops only in the matrix and in the notch region, see Fig. 12(f), as observed in Fig. 10(d), but it did not localise yet for this configuration. A slight delamination is observed at the notch in Fig. 12(h), whilst is it still absent in the CT-scan, see Fig. 10(d), and experimentally appears slightly after, Fig. 10(e).

The stress and damage distributions during the evolution of the fibre bundle damaging process at configuration #2 are illustrated in Fig. 13. For the 0°-ply, the fibre bundle damage localises at the notch in Fig. 13(g) with values above the softening onset. Besides, the 0° split failure mode experimentally observed in Fig. 10(g) in the 0°-ply, is extending, see Fig. 13(e). The matrix damage in the 90°-ply, see Fig. 13(f), is extending and forms bands parallel to the fibre according to the transverse ply cracks failure mode experimentally observed in Fig. 10(g). Finally, the delamination zone has expended from the notch as seen in Fig. 13(h), but the propagation remains limited in comparison with the experimental observation of Fig. 10(g) and are actually in better agreement with the previous stage of Fig. 10(f). This is partly explained by the fact that the delamination zone evolves fast near the failure onset.

6. Conclusions

The strength of carbon fibre is commonly described by a Weibull distribution. According to the basic statistic theories, the strength of carbon fibre bundle was represented by a binomial distribution, which can be approximated by a Gaussian distribution when the number of fibres in a bundle is high. According to the experimental strain measurements of a broken fibre embedded in

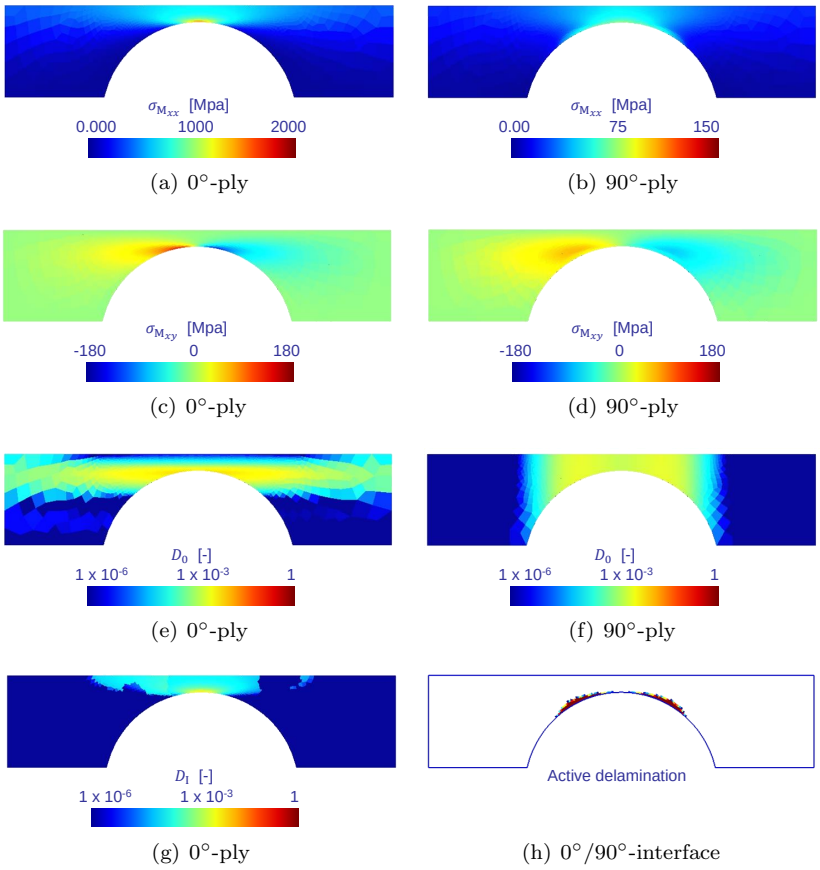

(a) 0°-ply (b) 90°-ply

(c) 0°-ply (d) 90°-ply

(e) 0°-ply (f) 90°-ply

(g) 0°-ply (h) 0°/90°-interface

Figure 12: Homogenised stress, damage and delamination distributions for tensile test of notched sample at configuration #1, see Fig. 11: (a-b) Homogenised tensile stress along the loading direction in the 0° and 90° plies; (c-d) Homogenised shear stress in the 0° and 90° plies; (e-f) Matrix damage (logarithmic scale) in the 0° and 90° plies; (g) Fibre bundle damage (logarithmic scale) in the 0° ply; and (h) Delaminated zones at the 0°-90° interface.

an epoxy matrix, an exponential relation was suggested to describe the longitudinal stress build-up profile developping along the fibre. Since the shape of the longitudinal stress build-up profile of a broken fibre is related to the maximum shear stress at the fibre-matrix interface and to the fibre radius, the length parameter of the Weibull fibre strength distribution could be determined from this maximum shear stress and the fibre radius. Higher fibre-matrix interface limit shear stress and smaller fibre radius lead to smaller length parameter L in the Weibull fibre strength distribution, which, in turn, leads to a higher longitudinal tensile strength of the composites. This result coincides with the experimentally observed phenomena.

The stochastic fibre bundle damage model was then introduced in a Mean

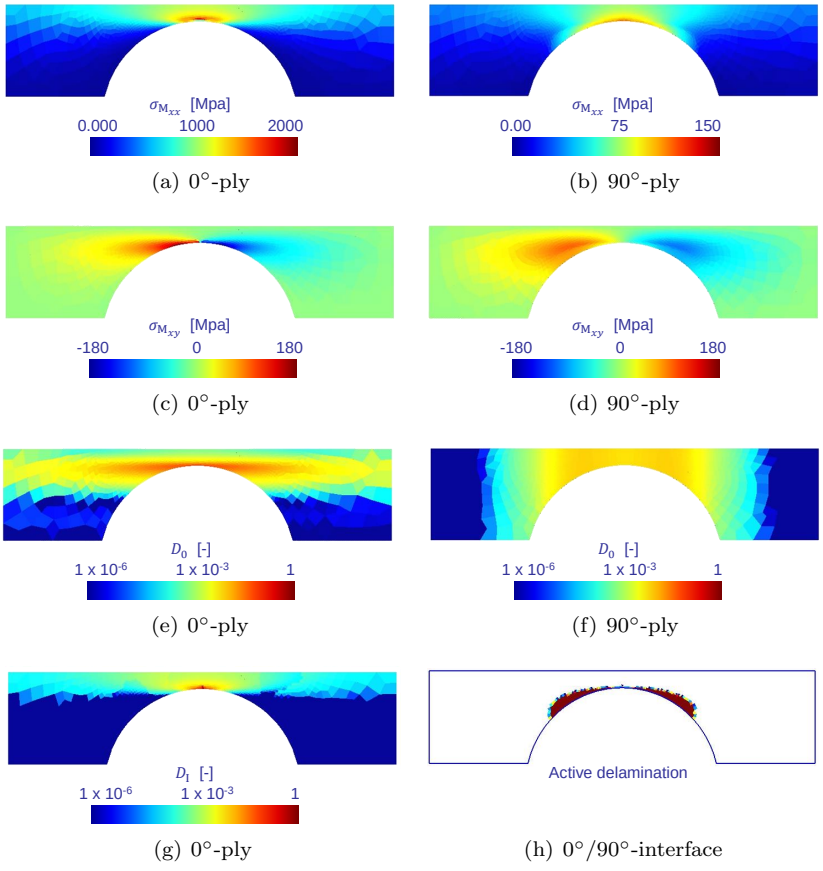

(a) 0°-ply (b) 90°-ply

(c) 0°-ply (d) 90°-ply

(e) 0°-ply (f) 90°-ply

(g) 0°-ply (h) 0°/90°-interface

Figure 13: Homogenised stress, damage and delamination distributions for tensile test of notched sample at configuration #2, see Fig. 11: (a-b) Homogenised tensile stress along the loading direction in the 0° and 90° plies; (c-d) Homogenised shear stress in the 0° and 90° plies; (e-f) Matrix damage (logarithmic scale) in the 0° and 90° plies; (g) Fibre bundle damage (logarithmic scale) in the 0° ply; and (h) Delaminated zones at the 0°-90° interface.

Field Homogenisation (MFH) extended to account for fibre bundle and matrix damaging processes of UD fibre reinforced composites. The uncertain damage enhanced Mori-Tanaka MFH was first used to study the effects of the fibres number and fibre volume fraction on the uncertain response of composites under longitudinal tension. Then, it was considered in a multi-scale finite element analysis of a sample to predict the longitudinal tensile strength of AS4/8552 unidirectional carbon fibre reinforced epoxy composite ply. The predicted strength agrees well with that of the reported value of the manufacturer. Finally, the damage enhanced MFH was applied in a finite element multi-scale simulation of a notched laminate under tensile loading. All the intra-laminar failure modes observed by an *in situ* experiment reported in the literature are well captured

by the damage variables related to the matrix and fibre bundle failure process. Delamination was also captured by an cohesive law introduced between the plies.

However, while the matrix cracking was formulated in an implicit-non-local form, thus alleviating mesh-dependency issues, the embedded fibre bundle damaging process was framed in a local form. Indeed, this work focuses on the micro-mechanics phase damage models, and their interactions, and will need to be extended in order to account explicitly for the fracture energy related to a longitudinal failure and to be mesh independent. To this end, since the embedded fibre bundle material model corresponds to an elastic damage model, it will be reformulated following a phase-field approach in [80]. Besides, in order to prevent high distortion of the elements for high values of damage, a damage to crack transition framework as considered in [91, 44, 92] will be carried out.

7. Acknowledgement

The research has been funded by the Walloon Region under the agreement n^o.7911-VISCOS in the context of the 21st SKYWIN call.

Data availability

The raw/processed data required to reproduce these findings cannot be shared at this time as the data also forms part of an ongoing study.

Appendix A. Material operators of the constitutive models

Appendix A.1. Matrix non-local damage model

In this section we complete the non-local damage model developed in Section 4.3 and summarise the derivation of the material operators in the incremental-form. Details can be found in [39]. For conciseness, the subscript "0" related to the matrix phase is omitted.

Appendix A.1.1. Plastic flow

During the plastic flow, $f = 0$ (29), $\dot{p}$ is positive, and the plastic strain tensor increment follows the normality rule

$$\dot{\boldsymbol{\varepsilon}}^{\mathrm{pl}} = \dot{p}\boldsymbol{N}_0\,, \quad \text{with} \quad \boldsymbol{N}_0 = \frac{\partial f}{\partial \hat{\boldsymbol{\sigma}}} = \frac{3}{2}\frac{\mathrm{dev}(\boldsymbol{\sigma})}{(1-D)\hat{\sigma}^{\mathrm{eq}}}\,, \tag{A.1}$$

where $\boldsymbol{N}_0$ is the normal to the yield surface in the effective stress space, and where the equivalent plastic strain $\dot{p} = [\frac{2}{3}\dot{\boldsymbol{\varepsilon}}^{\mathrm{pl}} : \dot{\boldsymbol{\varepsilon}}^{\mathrm{pl}}]^{1/2}$.

However, it has been shown in [37, 39] that the incremental-secant operator $\mathbb{C}_0^{\mathrm{Sr}}$ is naturally isotropic when considering the normal to the plastic flow from the residual state, *i.e.* when using $\boldsymbol{N} = \frac{3}{2}\frac{\mathrm{dev}(\hat{\boldsymbol{\sigma}}-\hat{\boldsymbol{\sigma}}_n^{\mathrm{res}})}{\sqrt{\frac{3}{2}\mathrm{dev}(\hat{\boldsymbol{\sigma}}-\hat{\boldsymbol{\sigma}}_n^{\mathrm{res}}):\mathrm{dev}(\hat{\boldsymbol{\sigma}}-\hat{\boldsymbol{\sigma}}_n^{\mathrm{res}})}}$ as a normal direction in Eq. (A.1). We note that in the case of the zero-incremental secant

that neglects the stress residual $\hat{\boldsymbol{\sigma}}_n^{\mathrm{res}}$, the normal in the return mapping is strictly the normal to the yield surface $\boldsymbol{N}_0$.

Assuming small deformations, the reversible (elastic) and irreversible (plastic) strain tensors can be added ($\boldsymbol{\varepsilon} = \boldsymbol{\varepsilon}^{\mathrm{el}} + \boldsymbol{\varepsilon}^{\mathrm{pl}}$), yielding

$$\boldsymbol{\sigma} = (1-D)\mathbb{C}^{\mathrm{el}} : (\boldsymbol{\varepsilon} - \boldsymbol{\varepsilon}^{\mathrm{pl}})\,, \tag{A.2}$$

where the fourth-order Hooke tensor of the undamaged material is given in Eq. (33).

Appendix A.1.2. Algorithmic material operators

In this section we summarise the material operators of the non-local constitutive law developed in Section 4.3.1.

In the case of the radial return mapping assumption, the derivative of the undamaged stress increment with respect to the strain increment reads (e.g. [93, chapter 12])

$$\mathbb{C}^{\mathrm{alg\,0}} = \frac{\mathrm{d}\Delta\hat{\boldsymbol{\sigma}}}{\mathrm{d}\Delta\boldsymbol{\varepsilon}} = \mathbb{C}^{\mathrm{el}} - \frac{(2\mu)^2}{h_0}\boldsymbol{N}_0 \otimes \boldsymbol{N}_0 - \frac{(2\mu)^2(\Delta p)}{\hat{\sigma}^{\mathrm{eq,\,tr}}}\left(\frac{3}{2}\mathbb{I}^{\mathrm{dev}} - \boldsymbol{N}_0 \otimes \boldsymbol{N}_0\right) \tag{A.3}$$

In this last relation, $\hat{\sigma}^{\mathrm{eq,\,tr}} = \sqrt{\frac{3}{2}\mathrm{dev}\,(\hat{\boldsymbol{\sigma}}^{\mathrm{tr}}) : \mathrm{dev}\,(\hat{\boldsymbol{\sigma}}^{\mathrm{tr}})}$ is the equivalent stress of the elastic predictor $\hat{\boldsymbol{\sigma}}^{\mathrm{tr}} = \hat{\boldsymbol{\sigma}}_n + \mathbb{C}^{\mathrm{el}} : \Delta\boldsymbol{\varepsilon}$ used in the radial return mapping, Δp is the accumulated plastic strain increment, the coefficient $h_0 = 3\mu + \frac{\mathrm{d}R}{\mathrm{d}p} > 0$ and the normal direction reads $\boldsymbol{N}_0 = \frac{3}{2}\frac{\mathrm{dev}(\hat{\boldsymbol{\sigma}})}{\hat{\sigma}^{\mathrm{eq}}}$, with $\hat{\sigma}^{\mathrm{eq}} = \sqrt{\frac{3}{2}\mathrm{dev}\,(\hat{\boldsymbol{\sigma}}) : \mathrm{dev}\,(\hat{\boldsymbol{\sigma}})}$.

In order to define the incremental-secant operator as isotropic, and in the case in which the residual was not neglected, the radial return mapping was modified to point to the residual stress, with $\boldsymbol{N} = \frac{3}{2}\frac{\mathrm{dev}(\hat{\boldsymbol{\sigma}}-\hat{\boldsymbol{\sigma}}_n^{\mathrm{res}})}{(\hat{\boldsymbol{\sigma}}-\hat{\boldsymbol{\sigma}}_n^{\mathrm{res}})^{\mathrm{eq}}}$, with $(\hat{\boldsymbol{\sigma}} - \hat{\boldsymbol{\sigma}}_n^{\mathrm{res}})^{\mathrm{eq}} = \sqrt{\frac{3}{2}\mathrm{dev}\,(\hat{\boldsymbol{\sigma}} - \hat{\boldsymbol{\sigma}}_n^{\mathrm{res}}) : \mathrm{dev}\,(\hat{\boldsymbol{\sigma}} - \hat{\boldsymbol{\sigma}}_n^{\mathrm{res}})}$. Eq. (A.3) thus becomes

$$\mathbb{C}^{\mathrm{alg\,r}} = \frac{\partial\Delta\hat{\boldsymbol{\sigma}}}{\partial\Delta\boldsymbol{\varepsilon}} = \mathbb{C}^{\mathrm{el}} - \frac{(2\mu)^2}{h}\boldsymbol{N} \otimes \boldsymbol{N} - \frac{(2\mu)^2(\Delta p)}{(\hat{\boldsymbol{\sigma}}^{\mathrm{tr}} - \hat{\boldsymbol{\sigma}}_n^{\mathrm{res}})^{\mathrm{eq}}}\left(\frac{3}{2}\mathbb{I}^{\mathrm{dev}} - \boldsymbol{N} \otimes \boldsymbol{N}\right) \tag{A.4}$$

with $h = 3\mu + \frac{1}{3}\boldsymbol{N} : \boldsymbol{N}_0^{-1}\frac{\mathrm{d}R}{\mathrm{d}p} > 0$. We note that h and $\boldsymbol{N}$ reduces respectively to h_0 and $\boldsymbol{N}_0$ when the residual stress vanishes.

In the following, $\mathbb{C}^{\mathrm{alg}}$ holds for either Eq. (A.3) or (A.4).

The material operators of the constitutive law (A.2) are then obtained, first for the derivatives of the Cauchy stress tensor, as

$$\mathbb{C}^{\varepsilon\varepsilon} = \frac{\mathrm{d}\Delta\boldsymbol{\sigma}}{\mathrm{d}\Delta\boldsymbol{\varepsilon}} = (1-D)\mathbb{C}^{\mathrm{alg}} - \hat{\boldsymbol{\sigma}} \otimes \frac{\partial D}{\partial\boldsymbol{\varepsilon}}\,, \tag{A.5}$$

$$\boldsymbol{C}^{\varepsilon\tilde{p}} = \frac{\mathrm{d}\Delta\boldsymbol{\sigma}}{\mathrm{d}\tilde{p}} = -\hat{\boldsymbol{\sigma}}\frac{\mathrm{d}D}{\mathrm{d}\tilde{p}}\,. \tag{A.6}$$

and then for the derivatives of the equivalent local plastic strain, as

$$\boldsymbol{C}^{p\varepsilon} = \frac{\mathrm{d}p}{\mathrm{d}\Delta\boldsymbol{\varepsilon}} = \frac{2\mu}{h_0}\boldsymbol{N_0} \quad \text{or } \boldsymbol{C}^{p\varepsilon} = \frac{2\mu}{h}\boldsymbol{N}\,, \tag{A.7}$$

$$C^{p\tilde{p}} = \frac{\mathrm{d}p}{\mathrm{d}\tilde{p}} = 0\,. \tag{A.8}$$

These expressions are completed by the linearisation of the damage law (32). During the damage increase, $\chi = \tilde{p}$ and one has

$$D = \frac{D_{\max}}{1 - \frac{1}{1+\exp(sp_{\rm C})}} \left(\frac{1}{1+\exp\left(-s(\tilde{p}-p_{\rm C})\right)} - \frac{1}{1+\exp\left(sp_{\rm C}\right)} \right) , \tag{A.9}$$

whose derivative reads

$$\delta D(\boldsymbol{\varepsilon},\ \tilde{p}) = \mathbf{0} : \delta\boldsymbol{\varepsilon} + \frac{D_{\max}}{1 - \frac{1}{1+\exp(sp_{\rm C})}} \left(\frac{s\exp\left(-s(\tilde{p}-p_{\rm C})\right)}{\left[1+\exp\left(-s(\tilde{p}-p_{\rm C})\right)\right]^2} \right) \delta\tilde{p} \, . \tag{A.10}$$

Appendix A.1.3. Derivatives of the incremental secant operator

For conciseness we omit the $\langle \bullet \rangle$ operator. The derivatives of the damaged incremental-secant operators (43) read [39]

$$\frac{\mathrm{d}\mathbb{C}^{\mathrm{S\,D}}}{\mathrm{d}\Delta\boldsymbol{\varepsilon}^{\mathrm{r}}} = (1-D)\frac{\mathrm{d}\mathbb{C}^{\mathrm{S}}}{\mathrm{d}\Delta\boldsymbol{\varepsilon}^{\mathrm{r}}} - \mathbb{C}^{\mathrm{S}} \otimes \frac{\mathrm{d}D}{\mathrm{d}\Delta\boldsymbol{\varepsilon}^{\mathrm{r}}} \, , \text{and} \tag{A.11}$$

$$\frac{\mathrm{d}\mathbb{C}^{\mathrm{S\,D}}}{\mathrm{d}\tilde{p}} = -\frac{\mathrm{d}D}{\mathrm{d}\tilde{p}}\mathbb{C}^{\mathrm{S}} \, , \tag{A.12}$$

with the derivative of the incremental-secant operators (41) reading

$$\frac{\mathrm{d}\mathbb{C}^{\mathrm{S}}}{\mathrm{d}\Delta\boldsymbol{\varepsilon}^{\mathrm{r}}} = 2\mathbb{I}^{\mathrm{dev}} \otimes \left[\frac{1}{6\mu^{\mathrm{S}}\left((\Delta\boldsymbol{\varepsilon}^{\mathrm{r}})^{\mathrm{eq}}\right)^2} \Delta\hat{\boldsymbol{\sigma}}^{\mathrm{r}} : \mathbb{I}^{\mathrm{dev}} : \mathbb{C}^{\mathrm{alg}} - \frac{2}{3}\mu^{\mathrm{S}} \frac{\mathbb{I}^{\mathrm{dev}} : \Delta\boldsymbol{\varepsilon}^{\mathrm{r}}}{\left((\Delta\boldsymbol{\varepsilon}^{\mathrm{r}})^{\mathrm{eq}}\right)^2} \right] , \tag{A.13}$$

with $(\Delta\boldsymbol{\varepsilon}^{\mathrm{r}})^{\mathrm{eq}} = \sqrt{\frac{2}{3}\mathrm{dev}(\Delta\boldsymbol{\varepsilon}^{\mathrm{r}}) : \mathrm{dev}(\Delta\boldsymbol{\varepsilon}^{\mathrm{r}})}$. In the case in which $\mathbb{C}^{\mathrm{Sr}}$ is used, $\mathbb{C}^{\mathrm{alg}}$ is obtained from Eq. (A.4), μ^{S} is defined by Eq. (37), and $\Delta\hat{\boldsymbol{\sigma}}^{\mathrm{r}} = \hat{\boldsymbol{\sigma}} - \hat{\boldsymbol{\sigma}}^{\mathrm{res}}$. In the case in which $\mathbb{C}^{\mathrm{S0}}$ is used, $\mathbb{C}^{\mathrm{alg}}$ is obtained from Eq. (A.3), μ^{S} is defined by Eq. (40), and $\Delta\hat{\boldsymbol{\sigma}}^{\mathrm{r}} = \hat{\boldsymbol{\sigma}}$. The damage derivatives follow from Eq. (A.10).

The derivative of the Eshelby tensor was developed in [39]:

$$\begin{aligned} \frac{\partial\mathbb{S}}{\partial\Delta\boldsymbol{\varepsilon}^{\mathrm{r}}} &= \frac{\partial\mathbb{S}}{\partial\nu} \otimes \left(\frac{\partial\nu}{\partial\kappa^{\mathrm{D}}}\frac{\partial\kappa^{\mathrm{D}}}{\partial\Delta\boldsymbol{\varepsilon}^{\mathrm{r}}} + \frac{\partial\nu}{\partial\mu^{\mathrm{S\,D}}}\frac{\partial\mu^{\mathrm{S\,D}}}{\partial\Delta\boldsymbol{\varepsilon}^{\mathrm{r}}} \right) \\ &= \frac{\partial\mathbb{S}}{\partial\nu} \otimes \left[\frac{\partial\nu}{\partial\kappa^{\mathrm{D}}} \left(-\kappa\frac{\partial D}{\partial\Delta\boldsymbol{\varepsilon}^{\mathrm{r}}} \right) + \right. \\ &\quad \left. \frac{\partial\nu}{\partial\mu^{\mathrm{S\,D}}} \left((1-D)\frac{\partial\mu^{\mathrm{S}}}{\partial\Delta\boldsymbol{\varepsilon}^{\mathrm{r}}} - \mu^{\mathrm{S}}\frac{\partial D}{\partial\Delta\boldsymbol{\varepsilon}^{\mathrm{r}}} \right) \right] , \end{aligned} \tag{A.14}$$

where $\frac{\partial\mu^{\mathrm{S}}}{\partial\Delta\boldsymbol{\varepsilon}^{\mathrm{r}}}$ is given in Eq. (A.13). Similarly, one has

$$\frac{\partial\mathbb{S}}{\partial\tilde{p}} = \frac{\partial\mathbb{S}}{\partial\nu} \otimes \left[\frac{\partial\nu}{\partial\kappa^{\mathrm{D}}} \left(-\kappa\frac{\partial D}{\partial\tilde{p}} \right) + \frac{\partial\nu}{\partial\mu^{\mathrm{S\,D}}} \left(-\mu^{\mathrm{S}}\frac{\partial D}{\partial\tilde{p}} \right) \right] . \tag{A.15}$$

Appendix A.2. Embedded fibre damage model

In this section we summarise the derivation of the material operators in the incremental-form for the local damage model developed in Section 4.4. For conciseness, the subscript "I" related to the inclusion phase and the operator $\langle\bullet\rangle$ are omitted.

Appendix A.2.1. Algorithmic material operators

The derivative of the constitutive material law (49) developed in Section 4.4.2 results in the algorithmic material operator

$$\mathbb{C}^{\varepsilon\varepsilon} = \frac{\mathrm{d}\boldsymbol{\sigma}}{\mathrm{d}\boldsymbol{\varepsilon}} = \frac{\mathrm{d}}{\mathrm{d}\boldsymbol{\varepsilon}}(\mathbb{C}^{\mathrm{D}} : \boldsymbol{\varepsilon}) = \mathbb{C}^{\mathrm{D}} + \boldsymbol{\varepsilon} : \frac{\mathrm{d}\mathbb{C}^{\mathrm{D}}}{\mathrm{d}D} \otimes \frac{\mathrm{d}D}{\mathrm{d}\boldsymbol{\varepsilon}}\,, \tag{A.16}$$

where the derivative of $\mathbb{C}^{\mathrm{D}}$ expressed in the in Voigt notation reads

$$\frac{\mathrm{d}\mathbf{C}^{\mathrm{D}}}{\mathrm{d}D} = \begin{bmatrix} \frac{\mathrm{d}C^{\mathrm{D}}_{11}}{\mathrm{d}D} & \frac{\mathrm{d}C^{\mathrm{D}}_{12}}{\mathrm{d}D} & \frac{\mathrm{d}C^{\mathrm{D}}_{13}}{\mathrm{d}D} & 0 & 0 & 0 \\ \frac{\mathrm{d}C^{\mathrm{D}}_{21}}{\mathrm{d}D} & \frac{\mathrm{d}C^{\mathrm{D}}_{22}}{\mathrm{d}D} & \frac{\mathrm{d}C^{\mathrm{D}}_{23}}{\mathrm{d}D} & 0 & 0 & 0 \\ \frac{\mathrm{d}C^{\mathrm{D}}_{31}}{\mathrm{d}D} & \frac{\mathrm{d}C^{\mathrm{D}}_{32}}{\mathrm{d}D} & \frac{\mathrm{d}C^{\mathrm{D}}_{33}}{\mathrm{d}D} & 0 & 0 & 0 \\ 0 & 0 & 0 & 0 & 0 & 0 \\ 0 & 0 & 0 & 0 & 0 & 0 \\ 0 & 0 & 0 & 0 & 0 & 0 \end{bmatrix}, \tag{A.17}$$

with the expressions of $\frac{\mathrm{d}C^{\mathrm{D}}_{ij}}{\mathrm{d}D}$, $(i,j=1,2,3)$ as detailed here below.

According to the definitions of damaged transverse isotropic tensor, Eq. (50), and of $\Delta^{\mathrm{D}} = (1+\nu^{1\,2})(1-\nu^{1\,2}-2\nu^{1\,3}\nu^{3\,1\,\mathrm{D}})$ with $\nu^{3\,1\,\mathrm{D}} = (1-D)\nu^{3\,1}$ and $E^{3\,\mathrm{D}} = (1-D)E^3$, one has

$$\begin{aligned}
\frac{\mathrm{d}C^{\mathrm{D}}_{11}}{\mathrm{d}D} &= \frac{\mathrm{d}C^{\mathrm{D}}_{22}}{\mathrm{d}D} = \frac{E^1\nu^{1\,3}\nu^{3\,1}}{\Delta^{\mathrm{D}}} - \frac{E^1(1-\nu^{1\,3}\nu^{3\,1\,\mathrm{D}})}{\Delta^{\mathrm{D}\,2}}\frac{\mathrm{d}\Delta^{\mathrm{D}}}{\mathrm{d}D}\,, \\
\frac{\mathrm{d}C^{\mathrm{D}}_{12}}{\mathrm{d}D} &= \frac{\mathrm{d}C^{\mathrm{D}}_{21}}{\mathrm{d}D} = -\frac{E^1\nu^{1\,3}\nu^{3\,1}}{\Delta^{\mathrm{D}}} - \frac{E^1(\nu^{1\,2}+\nu^{1\,3}\nu^{3\,1\,\mathrm{D}})}{\Delta^{\mathrm{D}\,2}}\frac{\mathrm{d}\Delta^{\mathrm{D}}}{\mathrm{d}D}\,, \\
\frac{\mathrm{d}C^{\mathrm{D}}_{13}}{\mathrm{d}D} &= \frac{\mathrm{d}C^{\mathrm{D}}_{31}}{\mathrm{d}D} = \frac{\mathrm{d}C^{\mathrm{D}}_{23}}{\mathrm{d}D} = \frac{\mathrm{d}C^{\mathrm{D}}_{32}}{\mathrm{d}D} \\
&= -\frac{E^3(\nu^{1\,3}+\nu^{1\,2}\nu^{1\,3})}{\Delta^{\mathrm{D}}} - \frac{E^{3\,\mathrm{D}}(\nu^{1\,3}+\nu^{1\,2}\nu^{1\,3})}{\Delta^{\mathrm{D}\,2}}\frac{\mathrm{d}\Delta^{\mathrm{D}}}{\mathrm{d}D}\,, \\
\frac{\mathrm{d}C^{\mathrm{D}}_{33}}{\mathrm{d}D} &= -\frac{E^3(1-\nu^{1\,2}\nu^{1\,2})}{\Delta^{\mathrm{D}}} - \frac{E^{3\,\mathrm{D}}(1-\nu^{1\,2}\nu^{1\,2})}{\Delta^{\mathrm{D}\,2}}\frac{\mathrm{d}\Delta^{\mathrm{D}}}{\mathrm{d}D}\,,
\end{aligned} \tag{A.18}$$

with

$$\frac{\mathrm{d}\Delta^{\mathrm{D}}}{\mathrm{d}D} = 2\nu^{1\,3}\nu^{3\,1}(1+\nu^{1\,2})\,. \tag{A.19}$$

Finally, still considering the Voigt notations, using Eqs. (45) and (46) yields

$$\begin{aligned}\frac{\mathrm{d}D}{\mathrm{d}\boldsymbol{\varepsilon}^i} &= \frac{\mathrm{d}D}{\mathrm{d}\varphi}\frac{\mathrm{d}\varphi}{\mathrm{d}\hat{\sigma}^3}\frac{\mathrm{d}\hat{\sigma}^3}{\mathrm{d}\varepsilon^i} \\ &= \left(1+\varrho\frac{1-2\varphi}{2\sqrt{N\varphi(1-\varphi)}}\right)\frac{m}{\sigma_0}\left(\frac{L}{L_0}\right)^{\alpha}\left(\frac{\hat{\sigma}^3}{\sigma_0}\right)^{m-1}\times \\ &\quad \exp\left[-\left(\frac{L}{L_0}\right)^{\alpha}\left(\frac{\hat{\sigma}^3}{\sigma_0}\right)^{m}\right]\times {C^{\mathrm{el}}}_{3\,i}\,, \end{aligned} \tag{A.20}$$

where we have used the expression $\hat{\sigma}^3 = {C^{\mathrm{el}}}_{3\,i}\varepsilon^i$, with $i = 1, 2, 3$.

Appendix A.2.2. Derivatives of the incremental secant operator

Using Eq. (54), one has

$$\frac{\mathrm{d}\mathbb{C}^{\mathrm{S\,D}}}{\mathrm{d}\boldsymbol{\varepsilon}} = \frac{\mathrm{d}\mathbb{C}^{\mathrm{D}}}{\mathrm{d}\boldsymbol{\varepsilon}} = \frac{\mathrm{d}\mathbb{C}^{\mathrm{D}}}{\mathrm{d}D}\otimes\frac{\mathrm{d}D}{\mathrm{d}\boldsymbol{\varepsilon}}\,. \tag{A.21}$$

Appendix B. Delamination model

Because of the existence of the damaging process taking place in the matrix phase of the ply, the stresses are reduced in the presence of damage D_0, which could prevent the delamination initiation using a classical criterion. We thus use the delamination initiation criterion developed in [21]

$$\frac{\ll\sigma\gg^2}{\hat{\sigma}_{\mathrm{I\,C}}^2} + \frac{\tau^2}{\hat{\tau}_{\mathrm{II\,C}}^2} \leq (1-D_0)^2\,, \tag{B.1}$$

where $\sigma = \boldsymbol{n}\cdot\boldsymbol{\sigma}\cdot\boldsymbol{n}$ and $\tau = \sqrt{(\boldsymbol{n}\cdot\boldsymbol{\sigma})\cdot(\boldsymbol{n}\cdot\boldsymbol{\sigma}) - \sigma^2}$ are respectively the normal and tangent components of the apparent surface traction $\bar{\boldsymbol{t}} = \boldsymbol{\sigma}\cdot\boldsymbol{n}$ at the interface of unit normal $\boldsymbol{n}$, $\hat{\sigma}_{\mathrm{I\,C}}$ and $\hat{\tau}_{\mathrm{II\,C}}$ are the maximum tension and shearing of the cohesive model, and where the operator $\ll\bullet\gg$ refers to the positive value, *i.e.* is equal to zero in case of negative argument. The damage in the fibre bundle is not introduced in Eq. (B.2), because it usually triggers matrix damage as well. For simplicity, we redefine Eq. (B.1) as

$$\frac{\ll\sigma\gg^2}{\sigma_{\mathrm{I\,C}}^2} + \frac{\tau^2}{\tau_{\mathrm{II\,C}}^2} \leq 1\,, \tag{B.2}$$

with $\sigma_{\mathrm{I\,C}} = (1-D_0)\hat{\sigma}_{\mathrm{I\,C}}$ and $\tau_{\mathrm{II\,C}} = (1-D_0)\hat{\tau}_{\mathrm{II\,C}}$ the critical values at delamination onset.

Before delamination onset, the compatibility is constrained with the discountinous Galerkin method [21]. During delamination, we define the effective stress $\sigma_{\mathrm{eff}} = \sqrt{\ll\sigma\gg^2 + \tau^2}$ that governs the cohesive law in terms of the mixed mode opening Δ, which is evaluated from the opening $\boldsymbol{\delta}$ following

$$\Delta = \sqrt{\ll\delta_{\mathrm{I}}\gg^2 + (\delta_{\mathrm{II}})^2} = \begin{cases}\sqrt{1+\eta^2}\delta_{\mathrm{I}} & \text{if } \delta_{\mathrm{I}} > 0 \\ \delta_{\mathrm{II}} & \text{if } \delta_{\mathrm{I}} \leq 0\end{cases}\,, \tag{B.3}$$

where $\delta_{\mathrm{I}} = \boldsymbol{\delta} \cdot \boldsymbol{n}$, $\delta_{\mathrm{II}} = \|\boldsymbol{\delta} - \delta_{\mathrm{I}} \boldsymbol{n}\|$, and $\eta = \frac{\delta_{\mathrm{II}}}{\delta_{\mathrm{I}}}$. Before delamination, an initial stiffness K is used, so that

$$\sigma = K\delta_{\mathrm{I}} \text{ and } \tau = K\delta_{\mathrm{II}}\,. \tag{B.4}$$

Once Eq. (B.2) is satisfied, we define the values of δ_{I}, δ_{II}, σ_{eff}, σ, τ, and Δ at delamination onset respectively as δ_{I_0}, δ_{I_0}, and $\sigma_{\mathrm{eff}_0} = K\Delta_0$, $\sigma_0 = K\delta_{\mathrm{I}_0}$, $\tau_0 = K\delta_{\mathrm{I}_0}$ and Δ_0 with, using Eqs. (B.2) and (B.3),

$$\Delta_0 = \begin{cases} \frac{\sigma_{\mathrm{I\,C}}\tau_{\mathrm{II\,C}}\sqrt{1+\eta^2}}{K\sqrt{(\tau_{\mathrm{II\,C}})^2+(\eta\sigma_{\mathrm{I\,C}})^2}} & \text{if } \delta_I > 0 \\ \frac{\tau_{\mathrm{II\,C}}}{K} & \text{if } \delta_I \leq 0 \end{cases}. \tag{B.5}$$

During the delamination process, the opening and shearing between the two plies are governed by their corresponding energy release rates G_{I} and G_{II}, with a complete fracture obtained for

$$\left(\frac{G_{\mathrm{I}}}{G_{\mathrm{I\,C}}}\right)^{\alpha} + \left(\frac{G_{\mathrm{II}}}{G_{\mathrm{II\,C}}}\right)^{\alpha} = 1\,, \tag{B.6}$$

where $G_{\mathrm{I\,C}}$ and $G_{\mathrm{II\,C}}$ are the mode I and mode II critical energy release rates respectively, and where α is a mixed mode parameter. The evolution of σ_{eff} obeys to an exponential law in terms of the maximum reached opening $\Delta_{\max} = \max_{t' \leq t}(\Delta(t'))$ at time t, following

$$\sigma_{\mathrm{eff}} = \sigma_{\mathrm{eff}_0}\ \exp\left[-\beta_{\mathrm{eff}}\left(\frac{\Delta_{\max}}{\Delta_0} - 1\right)^{\xi}\right], \tag{B.7}$$

where ξ is a material parameter, and where β_{eff} will be computed to reach the sought critical energy release rate which satisfies Eq. (B.6). Since the delamination is irreversible, we introduce the parameter D_{coh} so that

$$\sigma_{\mathrm{eff}} = \begin{cases} (1 - D_{\mathrm{coh}})\, K\Delta & \text{if } \Delta \leq \Delta_{\max} \\ (1 - D_{\mathrm{coh}})\, \frac{\sigma_{\mathrm{eff}_0}}{\Delta_0}\Delta_{\max} & \text{if } \dot{\Delta} > 0 \text{ and } \Delta_{\max} = \Delta \end{cases}, \tag{B.8}$$

with the damage law

$$D_{\mathrm{coh}} = 1 - \frac{\Delta_0}{\Delta_{\max}} \exp\left[-\beta_{\mathrm{eff}}\left(\frac{\Delta_{\max}}{\Delta_0} - 1\right)^{\xi}\right]. \tag{B.9}$$

In order to evaluate β_{eff}, we define the critical opening $\delta_{\mathrm{I\,C}}$ and $\delta_{\mathrm{II\,C}}$ so that they are linked to their critical energy release rate as for a bilinear law. On the one hand, for pure mode loading, the critical openings are $\delta_{\mathrm{I\,C}} = \Delta_{\mathrm{I\,C}}$, $\delta_{\mathrm{II\,C}} = \Delta_{\mathrm{II,C}}$, with $G_{\mathrm{I\,C}} = \frac{\Delta_{\mathrm{I\,C}}\sigma_{\mathrm{I\,C}}}{2}$ and $G_{\mathrm{II\,C}} = \frac{\Delta_{\mathrm{II\,C}}\tau_{\mathrm{II\,C}}}{2}$. Using Eq. (B.8), this yields $\Delta_{\mathrm{I\,C}} = \delta_{\mathrm{I}_0}(1 + 2I)$ and $\Delta_{\mathrm{II\,C}} = \delta_{\mathrm{II}_0}(1 + 2I)$ where $I = \int_1^{+\infty} \exp\left[-\beta_{\mathrm{eff}}\,(x-1)^{\xi}\right] dx$. We also have $I = \frac{\Gamma\left(\frac{1}{\xi}\right)}{\xi\beta_{\mathrm{eff}}^{\frac{1}{\xi}}}$, with the Gamma function $\Gamma(z) = \int_0^{+\infty} e^{-x}x^{z-1}\,dx$. This yield the value of $\beta_{\mathrm{eff}} = \left[\frac{2\delta_{\mathrm{I}_0}}{\Delta_{\mathrm{I\,C}} - \delta_{\mathrm{I}_0}}\frac{\Gamma\left(\frac{1}{\xi}\right)}{\xi}\right]^{\xi}$ in pure mode I in oder to dissipate $G_{\mathrm{I\,C}}$ and similarly for pure mode II.

On the other hand, for mixed mode loading, we have at failure the energy release rates $G_{\mathrm{I}} = \frac{\sigma_0 \delta_{\mathrm{I\,C}}}{2}$ and $G_{\mathrm{II}} = \frac{\tau_0 \delta_{\mathrm{II\,C}}}{2}$, and we set $\delta_{\mathrm{I\,C}} = \gamma \delta_{\mathrm{I}_0}(1+2I)$ and $\delta_{\mathrm{II\,C}} = \gamma \delta_{\mathrm{II}_0}(1+2I)$, where γ has to be defined to respect Eq. (B.6). Using the above definitions, we have $\frac{G_{\mathrm{II}}}{G_{\mathrm{I}}} = \eta^2$, which combined to Eq. (B.6) yields $\delta_{\mathrm{I\,C}} = \frac{2\sqrt{1+\eta^2}}{\sigma_{\mathrm{eff}0}} \left[\left(\frac{1}{G_{\mathrm{I\,C}}} \right)^{\alpha} + \left(\frac{\eta^2}{G_{\mathrm{II\,C}}} \right)^{\alpha} \right]^{-\frac{1}{\alpha}}$ and $\delta_{\mathrm{II\,C}} = \eta \delta_{\mathrm{I\,C}}$. Eventually, the equivalent critical opening Δ_{C} to a bilinear law for a mixed loading mode is defined as

$$G_{\mathrm{eff}} = \begin{cases} \frac{1}{2}\sigma_{\mathrm{eff}_0}\Delta_{\mathrm{C}} & \text{if } \delta_{\mathrm{I}} > 0 \\ G_{\mathrm{II\,C}} & \text{if } \delta_{\mathrm{I}} \leq 0 \end{cases}, \tag{B.10}$$

with, following the above definitions,

$$\Delta_{\mathrm{C}} = \begin{cases} \sqrt{\left(\delta_{\mathrm{I\,C}}\right)^2 + \left(\delta_{\mathrm{II\,C}}\right)^2} & \text{if } \delta_{\mathrm{I}} > 0 \\ \frac{2G_{\mathrm{II\,C}}}{\tau_{\mathrm{II\,C}}} & \text{if } \delta_{\mathrm{I}} \leq 0 \end{cases}. \tag{B.11}$$

The effective material parameters required to dissipate the sought amount of energy are

$$\beta_{\mathrm{eff}} = \begin{cases} \left[\frac{2\Delta_0}{\Delta_{\mathrm{C}} - \Delta_0} \frac{\Gamma(\frac{1}{\xi})}{\xi} \right]^{\xi} & \text{if } \delta_{\mathrm{I}} > 0 \\ \left[\frac{2\Delta_0}{\Delta_{\mathrm{II\,C}} - \Delta_0} \frac{\Gamma(\frac{1}{\xi})}{\xi} \right]^{\xi} & \text{if } \delta_{\mathrm{I}} \leq 0 \end{cases}. \tag{B.12}$$

In this work we consider, $K = 10^{16}\mathrm{N} \cdot m^{-3}$, $\xi = 1.5$.

References

[1] I. J. Beyerlein, S. L. Phoenix, Statistics for the strength and size effects of microcomposites with four carbon fibers in epoxy resin, Composites Science and Technology 56 (1) (1996) 75 – 92. doi:10.1016/0266-3538(95)00131-X.

[2] S. Blassiau, A. Thionnet, A. Bunsell, Micromechanisms of load transfer in a unidirectional carbon fibrereinforced epoxy composite due to fibre failures. part 1: Micromechanisms and 3d analysis of load transfer: The elastic case, Composite Structures 74 (3) (2006) 303 – 318. doi:https://doi.org/10.1016/j.compstruct.2005.04.013.

[3] Y. Swolfs, L. Gorbatikh, I. Verpoest, Stress concentrations in hybrid unidirectional fibre-reinforced composites with random fibre packings, Composites Science and Technology 85 (2013) 10 – 16. doi:https://doi.org/10.1016/j.compscitech.2013.05.013.

[4] L. St-Pierre, N. J. Martorell, S. T. Pinho, Stress redistribution around clusters of broken fibres in a composite, Composite Structures 168 (2017) 226 – 233. doi:https://doi.org/10.1016/j.compstruct.2017.01.084.

[5] P. van den Heuvel, T. Peijs, R. Young, Failure phenomena in two-dimensional multifibre microcomposites: 3. a raman spectroscopic study of the influence of inter-facial debonding on stress concentrations, Composites Science and Technology 58 (1998) 933 – 944.

[6] P. van den Heuvel, S. Goutianos, R. Young, T. Peijs, Failure phenomena in fibre-reinforced composites. part 6: a finite element study of stress concentrations in unidirectional carbon fibre-reinforced epoxy composites, Composites Science and Technology 64 (5) (2004) 645 – 656. doi:https://doi.org/10.1016/j.compscitech.2003.06.003.

[7] A. Scott, M. Mavrogordato, P. Wright, I. Sinclair, S. Spearing, In situ fibre fracture measurement in carbonepoxy laminates using high resolution computed tomography, Composites Science and Technology 71 (12) (2011) 1471 – 1477. doi:https://doi.org/10.1016/j.compscitech.2011.06.004.

[8] J. Guerrero, J. Mayugo, J. Costa, A. Turon, A 3d progressive failure model for predicting pseudo-ductility in hybrid unidirectional composite materials under fibre tensile loading, Composites Part A: Applied Science and Manufacturing 107 (2018) 579 – 591. doi:https://doi.org/10.1016/j.compositesa.2018.02.005.

[9] T. Okabe, H. Sekine, K. Ishii, M. Nishikawa, N. Takeda, Numerical method for failure simulation of unidirectional fiber-reinforced composites with spring element model, Composites Science and Technology 65 (6) (2005) 921 – 933. doi:https://doi.org/10.1016/j.compscitech.2004.10.030.

[10] R. P. Tavares, F. Otero, A. Turon, P. P. Camanho, Effective simulation of the mechanics of longitudinal tensile failure of unidirectional polymer composites, International Journal of Fracture 208 (1) (2017) 269–285.

[11] R. P. Tavares, F. Otero, J. Baiges, A. Turon, P. P. Camanho, A dynamic spring element model for the prediction of longitudinal failure of polymer composites, Computational Materials Science 160 (2019) 42 – 52. doi:https://doi.org/10.1016/j.commatsci.2018.12.048.

[12] S. Pimenta, S. T. Pinho, Hierarchical scaling law for the strength of composite fibre bundles, Journal of the Mechanics and Physics of Solids 61 (6) (2013) 1337 – 1356. doi:https://doi.org/10.1016/j.jmps.2013.02.004.

[13] T.-T. Nguyen, D. Waldmann, T. Q. Bui, Role of interfacial transition zone in phase field modeling of fracture in layered heterogeneous structures, Journal of Computational Physics 386 (2019) 585–610. doi:https://doi.org/10.1016/j.jcp.2019.02.022.
URL https://www.sciencedirect.com/science/article/pii/S0021999119301391

[14] P. Zhang, W. Yao, X. Hu, T. Q. Bui, 3d micromechanical progressive failure simulation for fiber-reinforced composites, Composite Structures 249 (2020) 112534. doi:https://doi.org/10.1016/j.compstruct.2020.112534.
URL https://www.sciencedirect.com/science/article/pii/S0263822319348421

[15] R. P. Tavares, A. R. Melro, M. A. Bessa, A. Turon, W. K. Liu, P. P. Camanho, Mechanics of hybrid polymer composites: analytical and computational study, Computational Mechanics 57 (3) (2016) 405–421. doi:10.1007/s00466-015-1252-0.

[16] A. Dean, P. Asur Vijaya Kumar, J. Reinoso, C. Gerendt, M. Paggi, E. Mahdi, R. Rolfes, A multi phase-field fracture model for long fiber reinforced composites based on the puck theory of failure, Composite Structures 251 (2020) 112446. doi:https://doi.org/10.1016/j.compstruct.2020.112446.
URL http://www.sciencedirect.com/science/article/pii/S0263822320307078

[17] P. Zhang, X. Hu, T. Q. Bui, W. Yao, Phase field modeling of fracture in fiber reinforced composite laminate, International Journal of Mechanical Sciences 161-162 (2019) 105008. doi:https://doi.org/10.1016/j.ijmecsci.2019.07.007.
URL https://www.sciencedirect.com/science/article/pii/S0020740318341729

[18] P. Zhang, W. Yao, X. Hu, T. Q. Bui, An explicit phase field model for progressive tensile failure of composites, Engineering Fracture Mechanics 241 (2021) 107371. doi:https://doi.org/10.1016/j.engfracmech.2020.107371.
URL https://www.sciencedirect.com/science/article/pii/S0013794420309516

[19] T. Q. Bui, X. Hu, A review of phase-field models, fundamentals and their applications to composite laminates, Engineering Fracture Mechanics 248 (2021) 107705. doi:https://doi.org/10.1016/j.engfracmech.2021.107705.

[20] I. J. Beyerlein, S. Phoenix, Stress concentrations around multiple fiber breaks in an elastic matrix with local yielding or debonding using quadratic influence superposition, Journal of the Mechanics and Physics of Solids 44 (12) (1996) 1997 – 2039. doi:https://doi.org/10.1016/S0022-5096(96)00068-3.

[21] L. Wu, F. Sket, J. Molina-Aldareguia, A. Makradi, L. Adam, I. Doghri, L. Noels, A study of composite laminates failure using an anisotropic gradient-enhanced damage mean-field homogenization model, Composite Structures 126 (2015) 246 – 264. doi:https://doi.org/10.1016/j.compstruct.2015.02.070.

[22] P. Ponte Castañeda, J. Willis, The effect of spatial distribution on the effective behavior of composite materials and cracked media, Journal of the Mechanics and Physics of Solids 43 (12) (1995) 1919 – 1951. doi:10.1016/0022-5096(95)00058-Q.

[23] J. D. Eshelby, The determination of the elastic field of an ellipsoidal inclusion, and related problems, Proceedings of the Royal Society of London. Series A, Mathematical and Physical Sciences 241 (1226) (1957) pp. 376–396.

[24] T. Mori, K. Tanaka, Average stress in matrix and average elastic energy of materials with misfitting inclusions, Acta Metallurgica 21 (5) (1973) 571–574, cited By (since 1996) 1814.

[25] Y. Benveniste, A new approach to the application of Mori-Tanaka's theory in composite materials, Mechanics of Materials 6 (2) (1987) 147 – 157. doi:10.1016/0167-6636(87)90005-6.

[26] E. Kröner, Berechnung der elastischen konstanten des vielkristalls aus den konstanten des einkristalls, Zeitschrift für Physik A Hadrons and Nuclei 151 (1958) 504–518, 10.1007/BF01337948.

[27] R. Hill, A self-consistent mechanics of composite materials, Journal of the Mechanics and Physics of Solids 13 (4) (1965) 213 – 222. doi:10.1016/0022-5096(65)90010-4.

[28] R. Hill, Continuum micro-mechanics of elastoplastic polycrystals, Journal of the Mechanics and Physics of Solids 13 (2) (1965) 89 – 101. doi:10.1016/0022-5096(65)90023-2.

[29] D. R. S. Talbot, J. R. Willis, Variational principles for inhomogeneous nonlinear media, IMA Journal of Applied Mathematics 35 (1) (1985) 39–54. doi:10.1093/imamat/35.1.39.

[30] D. R. S. Talbot, J. R. Willis, Bounds and self-consistent estimates for the overall properties of nonlinear composites, IMA Journal of Applied Mathematics 39 (3) (1987) 215–240. doi:10.1093/imamat/39.3.215.

[31] P. Ponte Castañeda, The effective mechanical properties of nonlinear isotropic composites, Journal of the Mechanics and Physics of Solids 39 (1) (1991) 45–71. doi:10.1016/0022-5096(91)90030-R.

[32] P. Ponte Castañeda, A new variational principle and its application to nonlinear heterogeneous systems, SIAM Journal on Applied Mathematics 52 (5) (1992) 1321–1341.

[33] D. Talbot, J. Willis, Some simple explicit bounds for the overall behaviour of nonlinear composites, International Journal of Solids and Structures 29 (14-15) (1992) 1981 – 1987. doi:10.1016/0020-7683(92)90188-Y.

[34] I. Doghri, A. Ouaar, Homogenization of two-phase elasto-plastic composite materials and structures: Study of tangent operators, cyclic plasticity and numerical algorithms, International Journal of Solids and Structures 40 (7) (2003) 1681 – 1712. doi:10.1016/S0020-7683(03)00013-1.

[35] A. Molinari, F. El Houdaigui, L. Tóth, Validation of the tangent formulation for the solution of the non-linear eshelby inclusion problem, International Journal of Plasticity 20 (2) (2004) 291 – 307. doi:10.1016/S0749-6419(03)00038-X.

[36] I. Doghri, L. Adam, N. Bilger, Mean-field homogenization of elasto-viscoplastic composites based on a general incrementally affine linearization method, International Journal of Plasticity 26 (2) (2010) 219 – 238. doi:10.1016/j.ijplas.2009.06.003.

[37] L. Wu, L. Noels, L. Adam, I. Doghri, A combined incremental–secant mean–field homogenization scheme with per–phase residual strains for elasto–plastic composites, International Journal of Plasticity 51 (2013) 80–102. doi:10.1016/j.ijplas.2013.06.006.

[38] L. Wu, L. Noels, L. Adam, I. Doghri, A multiscale mean-field homogenization method for fiber-reinforced composites with gradient-enhanced damage models, Computer Methods in Applied Mechanics and Engineering 233–236 (2012) 164–179. doi:10.1016/j.cma.2012.04.011.

[39] L. Wu, L. Noels, L. Adam, I. Doghri, An implicit-gradient-enhanced incremental-secant mean-field homogenization scheme for elasto-plastic composites with damage, International Journal of Solids and Structures 50 (24) (2013) 3843 – 3860. doi:10.1016/j.ijsolstr.2013.07.022.

[40] R. Peerlings, R. de Borst, W. Brekelmans, S. Ayyapureddi, Gradient-enhanced damage for quasi-brittle materials, Int. J. Numer. Meth. Engng 39 (1996) 3391–3403.

[41] M. Geers, Experimental analysis and computational modelling of damage and fracture, Ph.D. thesis, University of Technology, Eindhoven (Netherlands). (1997).

[42] R. de Borst, C. V. Verhoosel, Gradient damage vs phase-field approaches for fracture: Similarities and differences, Computer Methods in Applied Mechanics and Engineering 312 (2016) 78 – 94, phase Field Approaches to Fracture. doi:http://dx.doi.org/10.1016/j.cma.2016.05.015.
URL http://www.sciencedirect.com/science/article/pii/S0045782516303796

[43] C. Steinke, I. Zreid, M. Kaliske, On the relation between phase-field crack approximation and gradient damage modelling, Computational Mechanics 59 (5) (2017) 717–735. doi:10.1007/s00466-016-1369-9.
URL http://dx.doi.org/10.1007/s00466-016-1369-9

[44] J. Leclerc, L. Wu, V. D. Nguyen, L. Noels, A damage to crack transition model accounting for stress triaxiality formulated in a hybrid nonlocal implicit discontinuous galerkin-cohesive band model framework, International Journal for Numerical Methods in Engineering 113 (3) (2018) 374–410. arXiv:https://onlinelibrary.wiley.com/doi/pdf/10.1002/nme.5618, doi:10.1002/nme.5618.
URL https://onlinelibrary.wiley.com/doi/abs/10.1002/nme.5618

[45] F. van der Meer, L. Sluys, Continuum models for the analysis of progressive failure in composite laminates, Journal of Composite Materials 43 (20) (2009) 2131–2156. doi:10.1177/0021998309343054.

[46] Y. Zhao, G. Weng, Transversely isotropic moduli of two partially debonded composites, International Journal of Solids and Structures 34 (4) (1997) 493 – 507. doi:https://doi.org/10.1016/S0020-7683(96)00027-3.

[47] A. Jain, Y. Abdin, W. V. Paepegem, I. Verpoest, S. V. Lomov, Effective anisotropic stiffness of inclusions with debonded interface for eshelby-based models, Composite Structures 131 (2015) 692 – 706. doi:https://doi.org/10.1016/j.compstruct.2015.06.007.

[48] T. Hobbiebrunken, M. Hojo, T. Adachi, C. D. Jong, B. Fiedler, Evaluation of interfacial strength in cf/epoxies using fem and in-situ experiments, Composites Part A: Applied Science and Manufacturing 37 (12) (2006) 2248 – 2256, the 11th USJapan Conference on Composite Materials. doi:https://doi.org/10.1016/j.compositesa.2005.12.021.
URL http://www.sciencedirect.com/science/article/pii/S1359835X06000066

[49] V.-D. Nguyen, L. Wu, L. Noels, A micro-mechanical model of reinforced polymer failure with length scale effects and predictive capabilities. validation on carbon fiber reinforced high-crosslinked rtm6 epoxy resin, Mechanics of Materials 133 (2019) 193 – 213. doi:10.1016/j.mechmat.2019.02.017.

[50] H. L. Cox, The elasticity and strength of paper and other fibrous materials, British Journal of Applied Physics 3 (3) (1952) 72–79. doi:10.1088/0508-3443/3/3/302.

[51] P. van den Heuvel, M. Wubbolts, R. Young, T. Peijs, Failure phenomena in two-dimensional multi-fibre model composites: 5. a finite element study, Composites Part A: Applied Science and Manufacturing 29 (9) (1998) 1121 – 1135. doi:https://doi.org/10.1016/S1359-835X(98)00089-X.

[52] J. Segurado, J. Llorca, A numerical approximation to the elastic properties of sphere-reinforced composites, Journal of the Mechanics and Physics of Solids 50 (10) (2002) 2107 – 2121.

[53] M. Berveiller, A. Zaoui, An extension of the self-consistent scheme to plastically-flowing polycrystals, Journal of the Mechanics and Physics of Solids 26 (5-6) (1978) 325 – 344. doi:10.1016/0022-5096(78)90003-0.

[54] H. E. Pettermann, A. F. Plankensteiner, H. J. Böhm, F. G. Rammerstorfer, A thermo-elasto-plastic constitutive law for inhomogeneous materials based on an incremental Mori-Tanaka approach, Computers & Structures 71 (2) (1999) 197 – 214. doi:10.1016/S0045-7949(98)00208-9.

[55] I. Doghri, L. Tinel, Micromechanical modeling and computation of elasto-plastic materials reinforced with distributed-orientation fibers, International Journal of Plasticity 21 (10) (2005) 1919 – 1940. doi:10.1016/j.ijplas.2004.09.003.
URL http://www.sciencedirect.com/science/article/pii/S0749641904001706

[56] O. Pierard, I. Doghri, Study of various estimates of the macroscopic tangent operator in the incremental homogenization of elasto-plastic composites, International Journal for Multiscale Computational Engineering 4 (2006) 521–543.

[57] A. Molinari, G. Canova, S. Ahzi, A self consistent approach of the large deformation polycrystal viscoplasticity, Acta Metallurgica 35 (12) (1987) 2983–2994.

[58] R. Masson, M. Bornert, P. Suquet, A. Zaoui, An affine formulation for the prediction of the effective properties of nonlinear composites and polycrystals, J. Mech. Phys. Solids 48 (2000) 1203–1227.

[59] A. Zaoui, R. Masson, Modelling stress-dependent transformation strains of heterogeneous materials, in: Y. A. Bahei-El-Din, G. J. Dvorak, G. M. L. Gladwell (Eds.), IUTAM Symposium on Transformation Problems in Composite and Active Materials, Vol. 60 of Solid Mechanics and Its Applications, Springer Netherlands, 2002, pp. 3–15. doi:10.1007/0-306-46935-9z_1.

[60] S. Mercier, A. Molinari, Homogenization of elasticviscoplastic heterogeneous materials: Self-consistent and Mori-Tanaka schemes, International Journal of Plasticity 25 (6) (2009) 1024 – 1048. doi:10.1016/j.ijplas.2008.08.006.
URL http://www.sciencedirect.com/science/article/pii/S0749641908001290

[61] J. Chaboche, P. Kanouté, A. Roos, On the capabilities of mean-field approaches for the description of plasticity in metal matrix composites, International Journal of Plasticity 21 (7) (2005) 1409 – 1434. doi:10.1016/j.ijplas.2004.07.001.

[62] P. Suquet, Overall properties of nonlinear composites: A modified secant moduli theory and its link with ponte castañeda's nonlinear variational procedure, Comptes Rendus de l" Académie des Sciences 320 (1995) 563–571.

[63] P. Ponte Castañeda, Exact second-order estimates for the effective mechanical properties of nonlinear composite materials, Journal of the Mechanics and Physics of Solids 44 (6) (1996) 827 – 862. doi:DOI:10.1016/0022-5096(96)00015-4.

[64] I. Doghri, L. Brassart, L. Adam, J. S. Gérard, A second-moment incremental formulation for the mean-field homogenization of elasto-plastic composites, International Journal of Plasticity 27 (3) (2011) 352 – 371. doi:DOI:10.1016/j.ijplas.2010.06.004.

[65] L. Wu, L. Adam, I. Doghri, L. Noels, An incremental-secant mean-field homogenization method with second statistical moments for elasto-visco-plastic composite materials, Mechanics of Materials 114 (2017) 180 – 200. doi:https://doi.org/10.1016/j.mechmat.2017.08.006.

[66] P. Ponte Castañeda, Second-order homogenization estimates for nonlinear composites incorporating field fluctuations: I - theory, Journal of the Mechanics and Physics of Solids 50 (4) (2002) 737 – 757. doi:10.1016/S0022-5096(01)00099-0.

[67] P. Ponte Castañeda, Second-order homogenization estimates for nonlinear composites incorporating field fluctuations: II - applications, Journal of the Mechanics and Physics of Solids 50 (4) (2002) 759 – 782. doi:10.1016/S0022-5096(01)00098-9.

[68] N. Lahellec, P. Suquet, On the effective behavior of nonlinear inelastic composites: I. incremental variational principles, Journal of the Mechanics and Physics of Solids 55 (9) (2007) 1932 – 1963. doi:10.1016/j.jmps.2007.02.003.

[69] N. Lahellec, P. Suquet, On the effective behavior of nonlinear inelastic composites: II. a second-order procedure, Journal of the Mechanics and Physics of Solids 55 (9) (2007) 1964 – 1992. doi:10.1016/j.jmps.2007.02.004.

[70] L. Brassart, L. Stainier, I. Doghri, L. Delannay, A variational formulation for the incremental homogenization of elasto-plastic composites, Journal of the Mechanics and Physics of Solids 59 (12) (2011) 2455 – 2475. doi:10.1016/j.jmps.2011.09.004.

[71] L. Brassart, L. Stainier, I. Doghri, L. Delannay, Homogenization of elasto-(visco) plastic composites based on an incremental variational principle, International Journal of Plasticity 36 (0) (2012) 86 – 112. doi:10.1016/j.ijplas.2012.03.010.

[72] N. Lahellec, P. Suquet, Effective response and field statistics in elasto-plastic and elasto-viscoplastic composites under radial and non-radial loadings, International Journal of Plasticitydoi:10.1016/j.ijplas.2012.09.005.

[73] J. Boudet, F. Auslender, M. Bornert, Y. Lapusta, An incremental variational formulation for the prediction of the effective work-hardening behavior and field statistics of elasto-(visco)plastic composites, International Journal of Solids and Structures 83 (2016) 90 – 113. doi:http://dx.doi.org/10.1016/j.ijsolstr.2016.01.003.
URL //www.sciencedirect.com/science/article/pii/S0020768316000068

[74] J. Lemaitre, Coupled elasto-plasticity and damage constitutive equations, Computer Methods in Applied Mechanics and Engineering 51 (1-3) (1985) 31 – 49. doi:10.1016/0045-7825(85)90026-X.

[75] J. Lemaitre, R. Desmorat, Engineering damage mechanics: ductile, creep, fatigue and brittle failures, Springer-Verlag, Berlin, 2005.

[76] I. Doghri, Numerical implementation and analysis of a class of metal plasticity models coupled with ductile damage, International Journal for Numerical Methods in Engineering 38 (20) (1995) 3403–3431. doi:10.1002/nme.1620382004.

[77] R. Peerlings, R. de Borst, W. Brekelmans, M. Geers, Gradient-enhanced damage modelling of concrete fracture, Mech. Cohesive-Frictional Mat. 3 (1998) 323–342.

[78] R. Peerlings, M. Geers, R. de Borst, W. Brekelmans, A critical comparison of nonlocal and gradient-enhanced softening continua, Int. J. Solids Structures 38 (2001) 7723–7746.

[79] M. Herráez, A. Fernández, C. S. Lopes, C. González, Strength and toughness of structural fibres for composite material reinforcement, Philos Trans A Math Phys Eng Sci. 374 (2071) (2016) 1–11. doi:https://doi.org/10.1098/rsta.2015.0274.

[80] L. Wu, T. Zhang, E. Maillard, L. Adam, P. Martiny, L. Noels, Per-phase spatial correlated damage models of ud fibre reinforced composites using mean-field homogenisation; application to model the yarn failure of plain woven composites, Computer & Structures.

[81] S. Pinho, L. Iannucci, P. Robinson, Formulation and implementation of decohesion elements in an explicit finite element code, Composites Part A: Applied Science and Manufacturing 37 (5) (2006) 778 – 789. doi:10.1016/j.compositesa.2005.06.007.

[82] A. Arteiro, G. Catalanotti, A. Melro, P. Linde, P. Camanho, Micro-mechanical analysis of the in situ effect in polymer composite laminates, Composite Structures 116 (2014) 827 – 840. doi:https://doi.org/10.1016/j.compstruct.2014.06.014.

[83] Hexcel Corporation, HexPly © 8552, Epoxy matrix (180°C/356°F curing matrix), Product Data Sheet (2016).

[84] Hexcel Corporation, HexTow © AS4, Carbon Fiber, Product Data Sheet (2018).

[85] V. Lucas, J.-C. Golinval, S. Paquay, V.-D. Nguyen, L. Noels, L. Wu, A stochastic computational multiscale approach; application to MEMS resonators, Computer Methods in Applied Mechanics and Engineering 294 (2015) 141 – 167. doi:http://dx.doi.org/10.1016/j.cma.2015.05.019.

[86] L. Wu, C. N. Chung, Z. Major, L. Adam, L. Noels, From sem images to elastic responses: a stochastic multiscale analysis of ud fiber reinforced composites, Composite Structures 0 (2018) 1 – 1. doi:http://dx.doi.org/10.1016/j.compstruct.

[87] E. Riks, On formulations of path-following techniques for structural stability analysis, NASA STI/Recon Technical Report N 931 (1992) 16346–+.

[88] M. G. D. Geers, Enhanced solution control for physically and geometrically non-linear problems. part iicomparative performance analysis, International Journal for Numerical Methods in Engineering 46 (2) (1999) 205–230. doi:10.1002/(SICI)1097-0207(19990920)46:2<205::AID-NME669>3.0.CO;2-S.
URL http://dx.doi.org/10.1002/(SICI)1097-0207(19990920)46:2<205::AID-NME669>3.0.CO;2-S

[89] A. Scott, I. Sinclair, S. Spearing, A. Thionnet, A. Bunsell, Damage accumulation in a carbon/epoxy composite: Comparison between a multiscale model and computed tomography experimental results, Composites Part A: Applied Science and Manufacturing 43 (9) (2012) 1514 – 1522. doi:https://doi.org/10.1016/j.compositesa.2012.03.011.

[90] L. Wu, V.-D. Nguyen, L. Adam, L. Noels, An inverse micro-mechanical analysis toward the stochastic homogenization of nonlinear random composites, Computer Methods in Applied Mechanics and Engineering 348 (2019) 97 – 138. doi:https://doi.org/10.1016/j.cma.2019.01.016.
URL http://www.sciencedirect.com/science/article/pii/S0045782519300210

[91] L. Wu, G. Becker, L. Noels, Elastic damage to crack transition in a coupled non-local implicit discontinuous galerkin/extrinsic cohesive law framework, Computer Methods in Applied Mechanics and Engineering 279 (2014) 379 – 409. doi:https://doi.org/10.1016/j.cma.2014.06.031.

URL http://www.sciencedirect.com/science/article/pii/S0045782514002175

[92] J. Leclerc, V.-D. Nguyen, T. Pardoen, L. Noels, A micromechanics-based non-local damage to crack transition framework for porous elastoplastic solids, International Journal of Plasticity 127 (2020) 102631. doi:10.1016/j.ijplas.2019.11.010.

[93] I. Doghri, Mechanics of Deformable Solids- Linear, Nonlinear, Analytical and Computational Aspects, Springer-Verlag, Berlin, 2000.